Monthly Notices
of the
ROYAL ASTRONOMICAL SOCIETY

MNRAS **473,** 1537–1553 (2018)
Advance Access publication 2017 September 22

doi:10.1093/mnras/stx2427

Lack of thermal energy in superbubbles: hint of cosmic rays?

Siddhartha Gupta,[1,2]★ Biman B. Nath,[1]★ Prateek Sharma[2] and David Eichler[3]

[1]*Raman Research Institute, Sadashiva Nagar, Bangalore 560080, India*
[2]*Joint Astronomy Programme, Department of Physics, Indian Institute of Science, Bangalore 560012, India*
[3]*Department of Physics, Ben-Gurion University, Be'er-Sheba 84105, Israel*

Accepted 2017 September 18. Received 2017 September 18; in original form 2017 May 26

ABSTRACT

Using analytic methods and 1D two-fluid simulations, we study the effect of cosmic rays (CRs) on the dynamics of interstellar superbubbles (ISBs) driven by multiple supernovae (SNe)/stellar winds in OB associations. In addition to CR advection and diffusion, our models include thermal conduction and radiative cooling. We find that CR injection at the reverse shock or within a central wind-driving region can affect the thermal profiles of ISBs and hence their X-ray properties. Even if a small fraction (10–20 per cent) of the total mechanical power is injected into CRs, a significant fraction of the ram pressure at the reverse shock can be transferred to CRs. The energy transfer becomes efficient if (1) the reverse shock gas Mach number exceeds a critical value ($M_{\rm th} \gtrsim 12$) and (2) the CR acceleration time-scale $\tau_{\rm acc} \sim \kappa_{\rm cr}/v^2$ is shorter than the dynamical time, where $\kappa_{\rm cr}$ is a CR diffusion coefficient and v is the upstream velocity. We show that CR affected bubbles can exhibit a volume-averaged hot gas temperature 1–5 $\times$ 10^6 K, lower by a factor of $2-10$ than without CRs. Thus, CRs can potentially solve the long-standing problem of the observed low ISB temperatures.

Key words: hydrodynamics – shock waves – ISM: bubbles – cosmic rays – galaxies: star clusters: general.

1 INTRODUCTION

Superbubbles driven by stellar winds and supernovae (SNe) from OB associations are the instruments of stellar feedback which regulate galaxy evolution. These expanding shells form the crucial link between stars and the interstellar medium (ISM) by depositing thermal and kinetic energy, and thereby influencing the star formation process. On a larger scale, they can launch galactic-scale outflows if certain conditions are fulfilled (Nath & Shchekinov 2013; Sharma et al. 2014).

The classical model of Weaver et al. (1977) provided the basic framework for wind driven bubbles. They described the shock structure expected in interstellar superbubbles (ISBs) and worked out the dynamics in the self-similar phase of evolution. Mac Low & McCray (1988) proposed an ISB model by considering correlated SNe and discussed its effects on the galactic scale. All these ideas have been studied in detail with numerical simulations (Keller et al. 2014; Vasiliev, Shchekinov & Nath 2017; Yadav et al. 2017).

In recent years, X-ray observations of various bubbles have led to a closer look into their dynamics (Townsley et al. 2006 and references therein). The presence of a dominant soft X-ray component at $\sim 2 \times 10^6$ K has also been highlighted in some of these studies (e.g. Chu et al. 2003; Maddox et al. 2009). Most of these studies provide the temperature and density of the X-ray emitting plasma which are often used to understand the effective driving force acting on the dense shell (Lopez et al. 2011; Pellegrini, Baldwin & Ferland 2011; Lopez et al. 2014). However, these analyses show that the best-fitting X-ray luminosity and temperature are often lower than that expected from the classical bubble model (Chu, Gruendl & Guerrero 2003; Harper-Clark & Murray 2009). Even with thermal conduction, which makes the bubble denser and cooler, the discrepancy is not fully resolved. Therefore, we investigate the role of cosmic rays (CRs) in modifying the ISB properties.

Supernova remnants also show results similar to ISBs. Chevalier (1983) re-examined the blast wave solution to model the effect of relativistic particles (see also Vink et al. 2010; Bell 2014). He showed that the injection of CRs can reduce the thermal energy inside the blast wave. This idea has been confirmed by analysing the post-shock temperature in a RCW 86 supernova remnant (Helder et al. 2009).

Recently, it has been suggested that ISBs are the preferred sites of CR acceleration instead of isolated supernova remnants (SNRs). Since massive stars usually form in clusters, most of the power injected by SNe into the ISM is mediated through superbubbles and not isolated SNRs (Higdon & Lingenfelter 2005). Binns et al. (2005) have suggested that the isotopic anomalies in the composition of Galactic cosmic rays, in particular, the enhanced $^{22}Ne/^{20}Ne$ ratio, are suggestive of CRs being accelerated out of the matter inside ISBs. Parizot & Drury (1999) argued that a superbubble model

★ E-mail: siddhartha@rri.res.in (SG); biman@rri.res.in (BBN)

for the origin of Galactic cosmic rays can explain the evolution of light elements Li, Be and B. Gamma-ray observations of the Cygnus superbubble have also shown that CRs are accelerated in ISBs (Ackermann et al. 2011). Recently Eichler (2017) has suggested that cosmic ray grammage traversed is correlated with the properties of the source, meaning that the escape occurs near the production site, suggestive of ISBs. Observations of extragalactic superbubbles in IC 10 (Heesen et al. 2014) and the Large Magellanic Cloud (Butt & Bykov 2008) have also suggested the ISB origin of CRs. Therefore, the dynamics of ISBs, and the possible effects of CRs on them, deserve to be studied in detail.

The role of CR feedback in galaxy evolution has also been discussed by several authors (e.g. Booth et al. 2013; Salem & Bryan 2013; Wiener, Pfrommer & Oh 2017). Although these studies included various physical processes e.g. self-gravity, cooling, and star formation, the effects of the individual processes are difficult to disentangle.

In this paper, we present a two-fluid model of ISB. We start with a standard ISB model and include thermal conduction, radiative cooling and CR diffusion one by one to understand the role of each process. We show that in the absence of CRs the thermal pressure of hot gas depends on the ambient density (almost independent of density profile) and the shell speed. Then we explore the effect of CRs. We have found that CRs can affect ISB via shock interactions and their effects mainly depend on the shock Mach number (Drury & Volk 1981; Becker & Kazanas 2001) and CR diffusion coefficient.

The contents of this paper are organized as follows. We present a broad analytical frame work in Section 2. The details of the simulation set-up are given in Section 3. The results from various runs are presented in Section 4. In Section 5, we discuss the dependence of the results on various parameters. In Section 6, we comment on the astrophysical implication of this study. Finally, we conclude in Section 7 by highlighting the main results of this paper.

2 ANALYTICAL PRELUDE

Consider the powerful wind from OB association is driving an ISB. The dynamics and the structure of an ISB are usually understood by the momentum and energy conservation equations:

$$\frac{\mathrm{d}}{\mathrm{d}t}(M\,\dot{R}) = 4\pi\,R^2\,P \tag{1}$$

$$\frac{\mathrm{d}}{\mathrm{d}t}\left(\frac{4}{3}\pi\,R^3\frac{P}{\gamma-1}\right) = L_\mathrm{w} - 4\pi\,R^2\,\dot{R}\,P - L_\mathrm{loss}, \tag{2}$$

where P is the pressure inside the bubble (assumed to be $\gg$ ambient pressure), R is the position of the swept-up ISM (hereafter 'shell') w.r.t. the central source,[1] $M = \int_0^R \mathrm{d}r\,4\,\pi\,r^2\,\rho(r)$ is the swept-up ambient mass, $\rho(r)$ is the ambient density (cf. equation 3), L_w is the wind power and L_loss is the loss of energy due to radiative cooling.

In order to find a general solution of equations (1) and (2), we choose the ambient density profile as

$$\rho(r) = \rho_\mathrm{c}\left(\frac{r_c}{r}\right)^s, \tag{3}$$

where the choice of the parameter 's' determines the ambient density profile. In next sections, we discuss the solutions in different cases.

[1] By the source region, we mean a region within which most of the stars are located, i.e. the region which is driving the ISB.

Table 1. The constant factors presented in equations (6) and (7).

γ	s	C_1	C_2	ξ
5/3	0.0	0.763	0.163	0.78
	1.0	0.607	0.285	0.83
	2.0	0.376	1.000	1.00
13/9	0.0	0.732	0.150	0.78
	1.0	0.580	0.272	0.83
	2.0	0.357	1.000	1.00
4/3	0.0	0.708	0.140	0.78
	1.0	0.558	0.262	0.83
	2.0	0.341	1.000	1.00

2.1 One-fluid standard ISB

2.1.1 Adiabatic evolution

Consider the case when the dynamical time (t_dyn) of an ISB is shorter than the cooling time-scales of its different regions (for details, see Castor, McCray & Weaver 1975, and sections 3 and 5.2 in Gupta et al. 2016). Under this assumption, the contribution of L_loss in the RHS of equation (2) is negligible. Assuming that at any given instant, $R \propto t_\mathrm{dyn}^\alpha$ (where $\alpha > 0$) and substituting P from equation (1) to equation (2), we obtain

$$R = C_1\,L_\mathrm{w}^{1/(5-s)}\,(\rho_\mathrm{c} r_\mathrm{c}^s)^{-1/(5-s)}\,t_\mathrm{dyn}^{3/(5-s)} \tag{4}$$

$$P = C_2\,L_\mathrm{w}^{(2-s)/(5-s)}\,(\rho_\mathrm{c} r_\mathrm{c}^s)^{3/(5-s)}\,t_\mathrm{dyn}^{-(4+s)/(5-s)}, \tag{5}$$

where

$$C_1 = \left[\frac{(\gamma-1)\,(5-s)^3\,(3-s)}{4\pi\,\{(63-18\,s)\gamma + s(2s+1) - 28\}}\right]^{1/(5-s)} \text{ and}$$

$$C_2 = \left[\frac{21-6s}{(5-s)^2(3-s)}\right] C_1^{(2-s)}. \tag{6}$$

Note that, the choice $s = 0$ corresponds to an ISB expanding in a uniform medium (Weaver et al. 1977).

The pressure P [the shocked wind (SW) pressure] given in equation (5) can be re-written in following form:

$$P = \xi\,\rho\,v_\mathrm{sh}^2, \tag{7}$$

where v_sh is the shell velocity (=dR/dt; see equation 4), ρ is the unshocked ISM density (i.e. the upstream density; equation 3) and $\xi = C_1^{(s-2)}\,C_2\,[(5-s)/3]^2$. The values of C_1, C_2 and ξ for different adiabatic constants (γ) and s are given in Table 1. Note that, ξ depends weakly on the density profile (s), and therefore equation (7) is a robust estimate of the interior pressure of an ISB.

Using equation (7), the position of the reverse shock can be readily obtained by equating the ram pressure and the gas pressure of the SW region. This gives

$$R_\mathrm{rs} = \left(\frac{1}{4\pi\xi}\right)^{1/2}\rho^{-1/2}\,\dot{M}^{1/2}\,v_\mathrm{w}^{1/2}\,v_\mathrm{sh}^{-1}, \tag{8}$$

where $\dot{M}$ is the mass-loss rate of the source and $v_\mathrm{w} \approx (2L_\mathrm{w}/\dot{M})^{1/2}$ (Chevalier & Clegg 1985, hereafter CC85) is the wind velocity. For a uniform ambient medium, the position of the reverse shock is given by

$$R_\mathrm{rs} = 2.45\,\rho_2^{-3/10}\,\dot{M}_{-4}^{1/2}\,L_{39}^{-1/5}\,v_3^{1/2}\,t_6^{2/5}\ \mathrm{pc}. \tag{9}$$

Here, $\rho_2 = \rho/(10^2\,m_\mathrm{H}\,\mathrm{cm}^{-3})$, $\dot{M}_{-4} = \dot{M}/(10^{-4}\,\mathrm{M}_\odot\,\mathrm{yr}^{-1})$, $L_{39} = L_\mathrm{w}/(10^{39}\,\mathrm{erg\,s}^{-1})$, $v_3 = v_\mathrm{w}/(10^3\,\mathrm{km\,s}^{-1})$ and $t_6 = t_\mathrm{dyn}/(1\,\mathrm{Myr})$.

Neglecting thermal conduction, the density of the shocked wind region ($\rho_{\rm sw}$) can be estimated by applying the shock jump condition at the reverse shock. This gives

$$\rho_{\rm sw} = \left(\frac{\gamma+1}{\gamma-1}\right) \xi\, \rho\, v_{\rm sh}^2\, v_{\rm w}^{-2} \tag{10}$$

$$T_{\rm sw} = \frac{2(\gamma-1)}{(\gamma+1)^2}\frac{\mu m_{\rm H}}{k_{\rm B}} v_{\rm w}^2. \tag{11}$$

If one uses a typical wind velocity $v_{\rm w} \sim 2000\,{\rm km\,s^{-1}}$ (Leitherer et al. 1999), then $T_{\rm sw} \approx 5\times10^7$ K, which is higher than the observed ISB temperatures. At these temperatures and densities, the electron and ion temperatures are equalized by Coulomb collisions.

2.1.2 *Thermal conduction*

Thermal conduction transfers heat from the hot bubble interior to the cooled shell, which causes the evaporation of the swept-up shell mass into the interior of the bubble (Cowie & McKee 1977). The detailed self-similar analysis of Weaver et al. (1977) showed that for a uniform ambient medium, thermal conduction decreases the temperature of the hot gas and enhances the density of the interior. Choosing the classical isotropic thermal conductivity $\kappa_{\rm th} = 6\times10^{-7}T^{5/2}$ cgs (Mac Low & McCray 1988), we have

$$\rho_{\rm sw,tc} \simeq 0.27\, L_{39}^{6/35}\rho_2^{19/35}t_6^{-22/35}\,[1-R_{\rm rs}/R_{\rm cd}]^{2/5}\, m_{\rm H}\,{\rm cm^{-3}} \tag{12}$$

$$T_{\rm sw,tc} \simeq 1.26\times10^7 L_{39}^{8/35}\rho_2^{2/35}\,t_6^{-6/35}\,[1-R_{\rm rs}/R_{\rm cd}]^{-2/5}\ {\rm K}. \tag{13}$$

The use of classical thermal conduction, however, can be questioned because the assumption of isotropy is not valid in the presence of magnetic field. Furthermore, at the early times, the mean free path of electrons ($\lambda_{\rm m}$) $\gtrsim$ the temperature gradient scale ($l_{\rm T}$), which can cause conduction to be saturated. Therefore, equations (12) and (13) represent the upper limiting case of thermal conduction.

2.1.3 *Radiative cooling*

For a radiative bubble, cooling can delay the formation of the reverse shock (see section 5.2 in Gupta et al. 2016). However, once it forms, the qualitative description remains the same as above but their quantitative results change because of the term $L_{\rm loss}$ (see equation 2). The cooling loss rate ($L_{\rm loss}$) is defined as

$$L_{\rm loss} = \int_0^R {\rm d}r\, 4\pi\, R^2 n_{\rm e} n_{\rm i}\Lambda_{\rm N}\,, \tag{14}$$

where $n_{\rm i}/n_{\rm e}$ is the electron/ion number density and $\Lambda_{\rm N}$ is the normalized [w.r.t. $(n_{\rm i}n_{\rm e})$] cooling rate.

Note that, although the contact discontinuity (hereafter 'CD') occupies a much smaller volume compared to the size of the bubble, the contribution of the term $L_{\rm loss}$ mainly comes from the CD, since this is the region where the temperature passes though the peak of the cooling curve. It can be shown that, if $t_{\rm dyn}$ is longer than the shell cooling time-scale [$\tau_{\rm shell}$; see equation (4) in Gupta et al. 2016] then the term $(L_{\rm w}-L_{\rm loss})$ in equation (2) can be approximated as $\eta L_{\rm w}$, where η ($\leq$1) can be thought of as an energy efficiency parameter. This parameter (η) depends mainly on the ambient density (see section 6.3 in Gupta et al. 2016). The expressions in equations (4) and (5) are accordingly changed by replacing $L_{\rm w}$ by $\eta L_{\rm w}$.

2.2 Two-fluid ISBs

The discussions so far have been confined to the case of one-fluid ISB. Here, we discuss the modifications due to CRs.

The effects of CRs depend on three main parameters: (1) the regions where CRs are accelerated/injected, (2) the fraction of energy which goes into CRs and (3) the CR diffusion coefficient. Note that all these parameters are uncertain and therefore we cover a range of models and parameters.

For CR affected ISBs, the interior gas can be considered as a mixture of thermal and non-thermal particles. It is useful to define an effective adiabatic index $\gamma_{\rm cr}(=4/3)<\gamma<\gamma_{\rm th}(=5/3)$ to infer the dynamics. The adiabatic index of the gas mixture depends on the fraction of the thermal and non-thermal (CR) particles in the gas, which may vary between different regions in the ISB. Moreover, the description becomes more complicated when CR diffusion is considered. For a preliminary understanding, we divide the discussion based on the CR injection region.

2.2.1 *Injection at the shocks*

Consider a scenario in which the CRs are accelerated at the forward shock (hereafter FS; equivalent to CR injection at FS). In this case, we do not expect to see any change in the interior because CRs do not penetrate CD. However, if CR acceleration happens at the reverse shock (hereafter RS) then CRs can diminish the thermal pressure in the SW region. It results in a decrease of SW temperature which reduces the effect of thermal conduction.

For injecting CR at the shock, a parameter is commonly used (Chevalier 1983; Bell 2014), which is defined as

$$w = \frac{p_{\rm cr}}{p_{\rm th}+p_{\rm cr}}, \tag{15}$$

where $p_{\rm cr}$ and $p_{\rm th}$ are the CR and thermal pressure, respectively. The implications for CR injection at shocks (with and without CR diffusion) are discussed in detail in Section 4.2.1.

2.2.2 *Injection at the source region*

CR injection in the source region presents a different scenario. In this case, it is assumed that some fraction of total deposited energy by stellar winds and/or SNe goes into CRs (Salem & Bryan 2013). Here, the injection parameter is defined as

$$\epsilon_{\rm cr} = \frac{E_{\rm cr}}{E_{\rm IN}}\,, \tag{16}$$

where $E_{\rm cr}$ is the energy deposited in CRs and $E_{\rm IN}$ is the total deposited energy.

The main difference between equations (15) and (16) is that the former parameter is defined at a shock whereas the latter one is defined at the source. Unlike the previous case, CR injection in the source region causes a free-wind CR pressure profile ($p_{\rm cr}$) which makes the bubble structure different from the standard one-fluid ISB.

To obtain CR profile in the free-wind region, one has to solve a two-fluid steady-state model along the lines of CC85. Inside the free wind, we expect that $p_{\rm cr}\propto\rho^{4/3}$ (adiabatic expansion of the wind), i.e. $p_{\rm cr}\propto r^{-8/3}$. The normalization constant depends on the fraction of energy injected as CRs and also on the input source parameters (see table 1 in CC85). Our numerical simulation shows the power-law profile, which is valid only in the absence of CR diffusion, and

can be written as

$$\frac{p_{\rm cr}}{\dot{M}^{1/2} L_{\rm w}^{1/2} R_{\rm src}^{-2}} \simeq 0.011\, \epsilon_{\rm cr} \left(\frac{r}{R_{\rm src}}\right)^{-8/3}, \quad (17)$$

where $R_{\rm src}$ is the radius of the source region.

As the free wind reaches the reverse shock, one does not have a one-fluid shock. Two-fluid shocks have been previously studied by several authors (Drury & Volk 1981; Drury & Falle 1986; Wagner, Falle & Hartquist 2007). CR diffusion plays a key role in a two-fluid shock. For some upstream parameters, CRs can diffuse across the shock and the downstream CR pressure can increase. The downstream CRs then diffuse further, which changes the upstream CR pressure. As a result, the CR particles cross the shock multiple times (which is also known as diffusive shock acceleration; Becker & Kazanas 2001) and CRs can modify the shock.

Drury & Volk (1981) showed that, for a two-fluid shock, parameters of the downstream fluid can have three possible solutions: (1) globally smooth, (2) discontinuous solution and (3) gas mediated sub-shock. Becker & Kazanas (2001) classified the solution parameter space based on the upstream gas and CR Mach numbers (see their equation 25), which are defined as $M_{\rm th} = v/a_{\rm th}$ and $M_{\rm cr} = v/a_{\rm cr}$, respectively, where $a_{\rm th} = \sqrt{\gamma_{\rm th} p_{\rm th}/\rho}$ and $a_{\rm cr} = \sqrt{\gamma_{\rm cr} p_{\rm cr}/\rho}$ are the adiabatic sound speed for the respective fluids. They showed that if the gas Mach number exceeds a critical value 12.3, then the downstream (post-shock) CR pressure dominates over thermal pressure and the shock structure is globally smooth (see their figs 8 and 16). We therefore estimate the reverse shock and forward shock Mach numbers to predict the shock structure.

In case of the reverse shock, the upstream wind velocity can be assumed to be the same as the wind velocity ($v_{\rm w}$) because the RS velocity $\ll v_{\rm w}$ (see equation 8). The upstream sound speed is estimated using the steady-state free-wind pressure and density profiles (CC85), which gives $a_{\rm th,rs} = 0.56(R_{\rm rs}/R_{\rm src})^{-2/3} \dot{M}^{-1/2} L_{\rm w}^{1/2}$. For the uniform ambient, this yields

$$M_{\rm th,rs} = \frac{v_{\rm w}}{a_{\rm th,rs}} \simeq 8.15\, \eta^{-2/15} R_{\rm src,pc}^{-2/3} \rho_2^{-1/5} \dot{M}_{-4}^{1/6} L_{39}^{1/30} t_6^{4/15}. \quad (18)$$

The most interesting thing about the RS is that the Mach number increases with time. Therefore, the RS is expected to show a globally smooth profile after a time-scale $\tau_{\rm cri}$. For a uniform ambient medium, we obtain

$$\tau_{\rm cri} \simeq 4.65\, \eta^{1/2} R_{\rm src,pc}^{5/2} \rho_2^{3/4} \dot{M}_{-4}^{-5/8} L_{39}^{-1/8}\ {\rm Myr}. \quad (19)$$

Note that, in equation (18) we have included the energy efficiency term η (discussed in Section 2.1.3). This shows that a radiative ISB can satisfy the critical Mach number criterion ($M_{\rm th,rs} > 12.3$) at an earlier time than the adiabatic ISB.

The forward shock (FS) Mach number can easily be found by assuming the ambient medium is at rest. This gives

$$M_{\rm th,fs} = \frac{v_{\rm sh}}{a_{\rm th,fs}} \simeq 10\, v_{\rm sh,2}\, a_{\rm th,1}^{-1}. \quad (20)$$

It is worth mentioning that depending on the ambient temperature, $M_{\rm th,\,fs}$ can exceed 12.3. Therefore, the FS can also show a globally smooth shock structure. However, note that the Mach number of the forward shock decreases with time.

The important point is that, for a globally smooth solution, the upstream kinetic energy is mostly transferred to the downstream CR pressure. This diminishes the thermal pressure and can change the density and temperature profiles of ISBs.

3 SIMULATION SET-UP

In order to study the detailed effects of CRs in ISBs, we have developed a 1D, two-fluid code which we call TFH (standing for two-fluid hydrodynamics) code. TFH solves the following set of equations:

$$\frac{\partial \rho}{\partial t} + \vec{\nabla}.(\rho\, \vec{v}) = S_\rho \quad (21)$$

$$\frac{\partial}{\partial t}(\rho\, \vec{v}) + \vec{\nabla}.(\rho\, \vec{v} \otimes \vec{v}) + \vec{\nabla}(p_{\rm th} + p_{\rm cr}) = 0 \quad (22)$$

$$\frac{\partial}{\partial t}(e_{\rm th} + e_{\rm k}) + \vec{\nabla}.\left[(e_{\rm th} + e_{\rm k})\, \vec{v}\right] + \vec{\nabla}.\left[\vec{v}\,(p_{\rm th} + p_{\rm cr})\right] = p_{\rm cr} \vec{\nabla}.\vec{v} - \vec{\nabla}.\vec{F}_{\rm tc} + q_{\rm eff}^{-} + S_{\rm e} \quad (23)$$

$$\frac{\partial e_{\rm cr}}{\partial t} + \vec{\nabla}.\left[e_{\rm cr}\, \vec{v}\right] = -p_{\rm cr} \vec{\nabla}.\vec{v} - \vec{\nabla}.\vec{F}_{\rm crdiff} + S_{\rm cr}. \quad (24)$$

Here, ρ is the mass density, $\vec{v}$ is the fluid velocity, $p_{\rm th}/p_{\rm cr}$ is the thermal/CR pressure, $e_{\rm k} = \rho\, v^2/2$ is the kinetic energy density, and $e_{\rm th} = p_{\rm th}/(\gamma_{\rm th} - 1)$ and $e_{\rm cr} = p_{\rm cr}/(\gamma_{\rm cr} - 1)$ are the thermal (gas) and CR energy densities, respectively (Drury & Volk 1981; Wagner et al. 2007; Pfrommer et al. 2017). The terms S_ρ, $S_{\rm th}$ and $S_{\rm cr}$ in equations (21), (23) and (24) represent mass and energy terms deposited by the driving source. $F_{\rm tc}$ and $F_{\rm crdiff}$ represent thermal conduction flux and CR diffusion flux, respectively. The term $q_{\rm eff}^{-}$ accounts for the radiative energy loss of the thermal gas. For simplicity, we exclude the gas heating due to CR streaming (Guo & Oh 2008).

Currently, TFH has two solvers: (1) a ZEUS-like solver (Stone & Norman 1992) which performs transport and source terms separately (hereafter TS; for details, see chapter 5 in Dullemond 2009[2]) and (2) an HLL solver (Toro, Spruce & Speares 1994; for details, see chapter 10 in Toro 2009). Both solvers use the finite volume method and are first order accurate. Because of the first order scheme, all runs are done with very high resolution (typical resolution is 0.05 pc). Since TFH performs a two-fluid simulation, we have defined an effective sound speed as $c_{\rm s,eff} = \sqrt{(\gamma_{\rm cr} p_{\rm cr} + \gamma_{\rm th} p_{\rm th})/\rho}$ to estimate the CFL time-step (Courant, Friedrichs & Lewy 1928). The CFL time-step is defined as

$$\Delta t_{\rm CFL} = ({\rm CFL\ number}) \times {\rm MIN}\left(\frac{\Delta x_{\rm i}}{u^{\rm i}_{\rm max}}\right), \quad (25)$$

where $\Delta x_{\rm i}$ is the separation between $i^{\rm th}$ and $(i+1)^{\rm th}$ grids, $u^{\rm i}_{\rm max} = {\rm MAX}(|S_{\rm L}|, |S_{\rm R}|)$, $S_{\rm L} = {\rm MIN}[(v^{\rm i-1} - c^{\rm i-1}_{\rm s,eff}), (v^{\rm i} - c^{\rm i}_{\rm s,eff})]$ and $S_{\rm R} = {\rm MAX}[(v^{\rm i-1} + c^{\rm i-1}_{\rm s,eff}), (v^{\rm i} + c^{\rm i}_{\rm s,eff})]$ is the maximum wave speed between the left and right moving waves from the interface. TFH has gone through various test problems and the comparisons with the publicly available code PLUTO (Mignone et al. 2007) are shown in Appendix A.

For the runs in this paper, we set the solver to TS (see Appendix B) and the CFL number to 0.2. The details of important runs are given in Table 2. In the following sections, we discuss the terms on the RHS of equations (21)–(24).

3.1 Ambient medium

We consider a uniform ambient density and temperature. The ambient temperature is chosen such that the thermal pressure is 1 eV cm^{-3}. For the runs with CRs, we set the CR pressure to 1 eV cm^{-3}

[2] See http://www.mpia.de/homes/dullemon/lectures/fluiddynamics.

Table 2. Details of the runs.

(1) Model	(2) No. of OB stars (N)	(3) ρ_c (m_H cm^{-3})	(4) Two-fluid	(5) Microphysics CR diffusion (crd)	Therm. Conduction (t)	Cooling (c)	(6) Simulation box details Box size [r_{min}, r_{max}]	Grids [n]
N3_d2	10^3	10^2	N	N	N	N	[0.1,400.1]	[8000]
N3_d2_t	10^3	10^2	N	N	Y	N	[0.1,300.1]	[6000]
N3_d2_c	10^3	10^2	N	N	N	Y	[0.1,300.1]	[6000]
N3_d2_c_t	10^3	10^2	N	N	Y	Y	[0.1,300.1]	[6000]
N3_d2_cr	10^3	10^2	Y	N	N	N	[0.1,400.1]	[8000]
N3_d2_crd	10^3	10^2	Y	Y	N	N	[0.1,1000.1]	[20 000]
N3_d2_crd_t	10^3	10^2	Y	Y	Y	N	[0.1,300.1]	[6000]
N3_d2_crd_c	10^3	10^2	Y	Y	N	Y	[0.1,1000.1]	[20 000]
N3_d2_crd_c_t	10^3	10^2	Y	Y	Y	Y	[0.1,500.1]	[10 000]
N3_d0_crd_c	10^3	1	Y	Y	N	Y	[0.1,1400.1]	[28 000]
N3_d3_crd_c	10^3	10^3	Y	Y	N	Y	[0.1,1000.1]	[20 000]
N2_d2_crd_c	10^2	10^2	Y	Y	N	Y	[0.1,1000.1]	[20 000]
N4_d2_crd_c	10^4	10^2	Y	Y	N	Y	[0.1,1000.1]	[20 000]

Note. The symbols 'N' and 'Y' denote that the processes are switched off and on, respectively. The nomenclature of the models can be illustrated with the help of an example: N3_d2_crd_c_t represents a run where the number of N_{OB} stars is 10^3, the ambient density is 100 m_H cm^{-3} and the evolution has been studied using two-fluid equations (cr) with cosmic ray diffusion (crd), radiative cooling (c) and thermal conduction (t).

(i.e. assuming equipartition between CRs and thermal gas). For all cases, the initial velocity of gas is set to zero. We assume the metallicity of the injected materials to be solar, $Z = Z_\odot$, the same as in the ambient gas, where $Z_\odot$ is the solar metallicity.

3.2 Mass and energy deposition

The source terms S_ρ and S_e/S_{cr} represent the deposited mass and thermal/CR energy per unit time per unit volume. We add mass and energy in a small region of radius $R_{src} = 1$ pc. The radius (R_{src}) has been chosen such that the energy loss rate is much less than the energy injection rate. This condition ensures that cooling at the initial stage will not suppress the production of strong shocks (for details, see section 4.2.1 in Sharma et al. 2014).

The mass-loss rate ($\dot{M}$) and the mechanical (wind) power of the source (L_w) are related to the star formation rate (SFR) in the cloud and lifetime of the individual stars. If M_{st} is the stellar mass in the cloud and N_{OB} is the number of OB stars with the main-sequence lifetime τ_{OB}, then the SFR can be assumed to be M_{st}/τ_{OB} (Mac Low & McCray 1988). Assuming $M_{st} \approx 50\, N_{OB}\, M_\odot$ and $\tau_{OB} \approx 30$ Myr, we get SFR $\simeq 1.67 \times 10^{-6}\, N_{OB}\, M_\odot$ yr^{-1}. We have also assumed that $\dot{M} = 0.3$ SFR and 10^{51} erg is the energy released in each supernova, which yields

$$\dot{M} \simeq 5 \times 10^{-4} \left(\frac{N_{OB}}{10^3}\right) \left(\frac{\tau_{OB}}{30\,\mathrm{Myr}}\right)^{-1} \mathrm{M_\odot\ yr^{-1}} \quad (26)$$

$$L_w \simeq 10^{39} \left(\frac{N_{OB}}{10^3}\right) \left(\frac{E_{SN}}{10^{51}\,\mathrm{erg}}\right) \left(\frac{\tau_{OB}}{30\,\mathrm{Myr}}\right)^{-1} \mathrm{erg\ s^{-1}}. \quad (27)$$

As in OB associations, the wind is produced by the cumulative effects of stars and SNe, we have continuously injected them in the source region. However, one can consider the source of energy in terms of SNe. For such a case, the time interval between consecutive SNe is equivalent to $\delta t_{SN} \simeq \tau_{OB}/N_{OB} = 0.03\,(N_{OB}/10^3)^{-1}$ Myr, and the total energy and mass deposited during that duration are 10^{51} erg and 15 $M_\odot$, respectively. Our choice gives the wind velocity $v \simeq \sqrt{(2L_w/\dot{M})} \approx 2500$ km s^{-1} which is consistent with Starburst99 (Leitherer et al. 1999) for a constant SFR or for a coeval star cluster.

To inject cosmic rays in the source region (cf. Section 4.2), we use a injection parameter ϵ_{cr} (see equation 16) to specify the fraction of the total input energy given to CR (Booth et al. 2013; Salem & Bryan 2013). Therefore, $S_\rho = \dot{M}/V_{src}$, $S_{th} = (1 - \epsilon_{cr})L_w/V_{src}$ and $S_{cr} = \epsilon_{cr} L_w/V_{src}$. For fiducial runs, whenever CR injection at the source is mentioned, we set $\epsilon_{cr} = 0.2$ otherwise it is set to zero. We explore the dependence of the results on various parameters in Section 5.

3.3 Cooling & Heating

TFH uses the operator splitting method to include radiative cooling and heating. We use standard definition of a cooling function as given below

$$q_{eff}^{-} = -\, n_i\, n_e\, \Lambda_N + \mathrm{Heating}, \quad (28)$$

where Λ_N is the normalized cooling function (CLOUDY; Ferland et al. 1998) and n_i/n_e is the electron/ion number density. The region where the cooling energy loss becomes comparable to its thermal energy, TFH sub-cycles cooling. The number of sub-steps depends on the stiffness of cooling. We artificially stop cooling when the gas temperature goes below 10^4 K. This corresponds to the shell temperature which is maintained due to the photoheating by the radiation field of the driving source (for details, see fig. 4 in Gupta et al. 2016).

3.4 Diffusion terms

Thermal conduction and CR diffusion are also treated using operator splitting. Note that, for stability, the diffusion terms can have a much smaller time-step compared to the CFL time-step. TFH handles this by performing sub-cycling at each CFL time-step.

3.4.1 Thermal conduction

The thermal conduction flux F_{tc} is defined as:

$$\vec{F}_{tc} = \chi\, \vec{F}_{classical}, \quad (29)$$

where $\vec{F}_{classical} = -\kappa_{th}\, \vec{\nabla} T$, $\kappa_{th} = C\, T^{5/2}$ is the coefficient of thermal conduction (Spitzer 1962) and C is chosen to be 6×10^{-7} in cgs unit. The factor χ in equation (29) limits the conduction flux

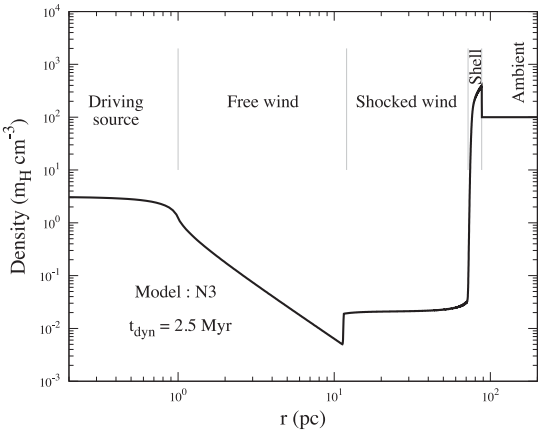

Figure 1. Density profile of a standard one-fluid ISB. The horizontal axis represents the distance from the driving source (r in pc) and the vertical axis displays the density. The snapshot is taken at $t_{\rm dyn} = 2.5$ Myr. For model details, see Table 2.

when it approaches $F_{\rm saturated} \approx (2\,k_{\rm B}\,T/\pi\,m_e)^{1/2}\,n_e k_{\rm B} T_e$ (Cowie & McKee 1977) and is defined as $\chi = F_{\rm saturated}/(|\vec{F}_{\rm classical}| + F_{\rm saturated})$.

The thermal conduction time-step ($\Delta t_{\rm tc}$) is chosen to be

$$\Delta t_{\rm tc} = \min_{\rm i} \left[\frac{\Delta x_{\rm i}^2}{2\,\kappa_{\rm th,avg}} \right], \tag{30}$$

where $\kappa_{\rm th,avg} = (\kappa_{\rm th,i-1} + \kappa_{\rm th,i})/2$ is the cell-averaged thermal conductivity.

3.4.2 CR diffusion

CR diffusion follows a similar method as thermal conduction (Section 2.1.2) except that the cosmic ray diffusion flux $F_{\rm crdiff}$ is defined as:

$$\vec{F}_{\rm crdiff} = -\kappa_{\rm cr}\vec{\nabla}\epsilon_{\rm cr}, \tag{31}$$

where $\kappa_{\rm cr}$ is the cosmic ray diffusion constant. Here, we are only concerned with the hydrodynamical effects of CRs, but one should remember that $\kappa_{\rm cr}$ is an integral over the CR energy distribution function (equation 7 in Drury & Volk 1981). We consider $\kappa_{\rm cr} = 5 \times 10^{26}\,{\rm cm^2\,s^{-1}}$ as a fiducial value which is consistent with the recent findings in the star forming/SNe region (e.g. Ormes, Özel & Morris 1988; Gabici et al. 2010; Giuliani et al. 2010; Li & Chen 2010; Ackermann et al. 2011) but smaller than the value usually adopted in the global ISM. We discuss the dependence of simulation results on this choice in Section 5.

4 RESULTS

4.1 An ideal one-fluid ISB

To begin with, we recall the structure of a standard ISB (Weaver et al. 1977). We run an ideal one-fluid model by turning off all microphysics (Table 2). Fig. 1 displays the density profile at $t_{\rm dyn} = 2.5$ Myr from this run.

Starting from the left, Fig. 1 shows that the ISB consists of four distinct regions: (1) the source region where mass and energy are deposited, (2) the free-wind region where the wind expands adiabatically, (3) the shocked-wind region and (4) the swept-up ambient medium shell. Between the regions (3) and (4), there is a contact discontinuity which separates the ambient material from the ejecta material.

In following sections, we include various microphysical processes one by one, for a better understanding of each process separately.

4.2 CR injection in different regions

4.2.1 At the forward/reverse shock

In supernova remnant studies, the downstream CR pressure fraction is taken as $p_{\rm cr} = w\,p_{\rm tot}$ (see equation 15), where the physical origin of w is poorly understood (Bell 2014). For the purpose of illustration, we choose $w = 1/2$. For implementing CR pressure fraction, we have written a shock detection module which identifies the shock location and fixes the CR pressure accordingly. We have tested this module by comparing it with the blast wave self-similar solution of Chevalier (1983) (see Appendix A2).

The results with CR injection at forward (top panel) and reverse (middle panel) shocks are displayed in Fig. 2. Black line stands for a standard one-fluid ISB (Section 4.1). The red curve represents the case where only CR advection is taken into account. For the blue curve, in addition to advection, CR diffusion has been turned on.

With injection at forward shock, in the absence of CR diffusion (red curve), a fraction of the post-shock thermal pressure appears as CR pressure. In this case, the contact discontinuity does not allow CR to be advected into the bubble, i.e. the total pressure in the shell remains the same. Therefore, it changes the effective adiabatic index of the swept-up shell ($\gamma_{\rm eff} = [5 + 3\,w]/[3(1 + w)]$), resulting in a higher density jump ($\simeq$5.5) compared to the one-fluid case (for which the compression ratio is 4). A more tangible difference appears when CR diffusion is turned on (blue curves). In this case, CRs enter inside the bubble and also diffuse out of the shell. Therefore, the total energy in the shell is now reduced. This results in a much higher density jump, similar to the case with radiative cooling.

In the middle panel of Fig. 2, CRs have been injected at the reverse shock. In the absence of CR diffusion (red curves), the CR pressure in the SW region remains almost the same as at the RS. As a result, the bubble size is slightly smaller than the standard bubble because of $\gamma_{\rm eff} = 13/9$. In this case, one can use an effective γ to determine the size of the bubble (see Table 1). However, this conclusion is not valid if one considers CR diffusion. With CR diffusion, the density jump at the RS is not sharp and the size of the bubble is smaller (compare the blue and black curves).

The conclusions from this section are: (1) the CR diffusion plays an important role and (2) the injection of CRs at the reverse shock can change the ISB structure.

4.2.2 At the driving source region

The numerical set-up for CR injection in a driving source region is discussed in Section 3.2 and the results are shown in the bottom panel of Fig. 2.

In absence of CR diffusion (red curves in panel (c) of Fig. 2), the free-wind CR pressure profile follows $p_{\rm cr} \propto r^{-8/3}$ (see equation 17). The grey line in the bottom right most panel of Fig. 2 displays this relation. The injected CR particles are advected up to the CD and the structure does not show any significant difference from that of the single-fluid case.

When diffusion is turned on [blue curves in panel (c)], we find that the CR pressure at the source region decreases, which

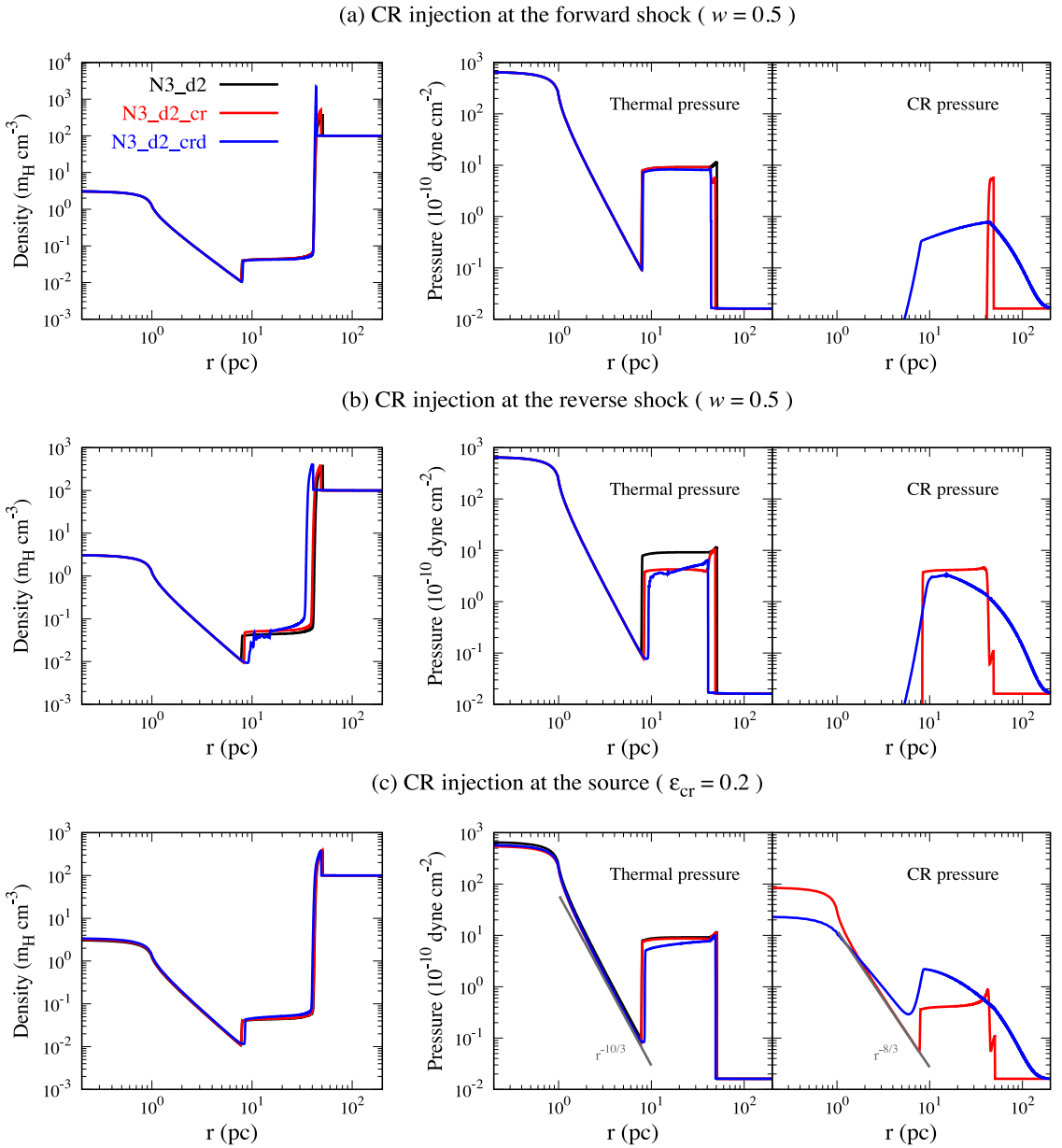

Figure 2. CR injection in different regions. Each row displays the density and thermal/CR pressure profiles for a specific injection model (Section 4.2) at $t_{\rm dyn} = 1$ Myr. The black curves in all panels represent a one-fluid bubble. The red and blue curves both stand for a two-fluid bubble, but CR diffusion ($\kappa_{\rm cr} = 5 \times 10^{26}\,{\rm cm^2\,s^{-1}}$) is on only for the blue curve. The grey lines in panel (c) display the free-wind thermal pressure ($p_{\rm th} \propto r^{-10/3}$) and CR pressure ($p_{\rm cr} \propto r^{-8/3}$; equation 17) profiles. This figure highlights the role of CR diffusion and a self-consistent CR acceleration at the reverse shock (bottom row).

is expected because CRs diffuse from the high to low pressure region. The striking feature is that, at the RS, the CR pressure is quite large compared to the case of no diffusion. This jump in CR pressure is a property of two-fluid shocks as discussed in Section 2.2.2.

Fig. 3 displays the time evolution of the reverse shock Mach number for three different values of $N_{\rm OB}$, where the blue colour stands for our fiducial choice. The solid lines in this figure display the analytical estimate of the RS gas Mach number (equation 18) and the blue circles represent the numerical results obtained from our fiducial run. This model shows that the RS satisfies the globally smooth condition after $t_{\rm dyn} \approx 1.7$ Myr. The Mach number analysis for the FS shows that at early times, the FS also satisfies $M_{\rm th} > 12.3$ (not displayed in this figure). However in our simulations, we do not see a globally smooth shock at the FS. The reason is discussed as follows.

For a large post-shock CR pressure, i.e. for efficient CR acceleration, the CR particles should cross the shock multiple times. Becker & Kazanas (2001) found the critical Mach number for CR dominated post-shock in a steady state. A steady state assumes that CR particles have sufficient time to cross the shock multiple times. For a time-dependent calculation, we must consider a CR acceleration time-scale ($\tau_{\rm acc}$). Drury (1983) discussed that if Δt is the average time taken by the upstream CR particles to cross the shock and to return back from downstream (thereby, CRs complete one cycle), and $\Delta\mathcal{P}$ is the average momentum gain in one complete

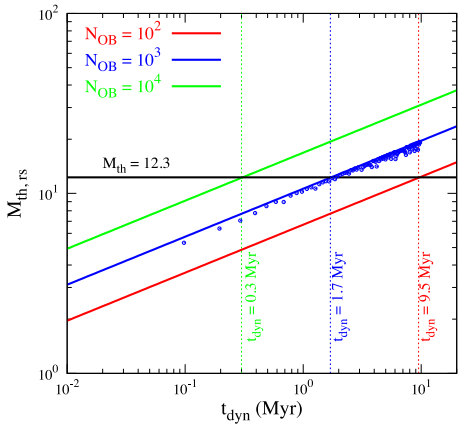

Figure 3. Gas Mach number of the reverse shock as a function of dynamical time for three different $N_{\rm OB}$. The black line shows the critical Mach number for the globally smooth solution. The blue curve represents our fiducial model (also see equation 18) and the blue points show the data points from our simulation. This figure implies that, for large $N_{\rm OB}$, the globally smooth solution is achieved at early times.

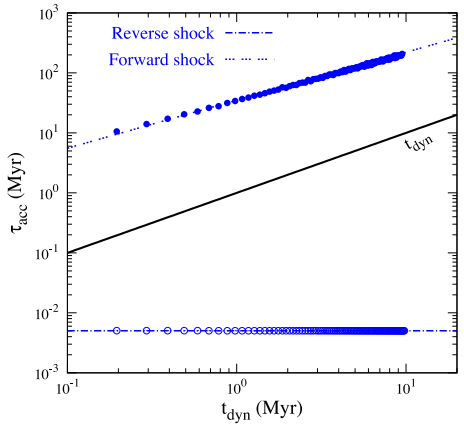

Figure 4. The CRs acceleration time-scale at the reverse shock and the forward shock as a function of dynamical time. The black line shows the dynamical time. The dashed and dashed-dotted blue lines are the analytic estimates from equation (32). The blue solid and empty circles show results from our simulation. Figure shows that, at the FS, $\tau_{\rm acc}$ is always greater than $t_{\rm dyn}$ explaining the reason for not seeing CR dominated smooth FS.

cycle, then

$$\tau_{\rm acc} = \frac{\mathcal{P}_1}{\Delta\mathcal{P}/\Delta t} = \frac{3}{v_1 - v_2}\left(\frac{\kappa_{\rm cr,1}}{v_1} + \frac{\kappa_{\rm cr,2}}{v_2}\right), \tag{32}$$

where subscripts 1 and 2 stand for the upstream and downstream flow, respectively (also see Blasi, Amato & Caprioli 2007). Therefore, we can see the globally smooth solution only if $\tau_{\rm acc} \ll \tau_{\rm cri} < t_{\rm dyn}$.

Equation (32) can be written as $\tau_{\rm acc} \sim 6\,\kappa_{\rm cr}/v_1^2$ (≡CR diffusion time-scale). For the FS and RS, the condition $t_{\rm dyn} \gg \tau_{\rm acc}$ yields

$$\text{Forward shock}: t_{\rm dyn} \gg 11\,\kappa_{26}^{5}\,L_{39}^{-2}\,\rho_2^{2}\ \text{Myr}, \tag{33}$$

$$\text{Reverse shock}: t_{\rm dyn} \gg 2\times10^{-3}\,\kappa_{26}\,v_3^{-2}\ \text{Myr}, \tag{34}$$

where we have taken v_1 as the FS velocity in a uniform ambient medium ($\approx 0.6\,L_{\rm w}^{1/5}\,\rho^{-1/5}\,t_{\rm dyn}^{-2/5}$) and the wind velocity ($v_{\rm w}$), respectively. To illustrate this, we have estimated $\tau_{\rm acc}$ for the FS and RS (Model: N3_d2; Table 2) and the results are shown in Fig. 4.

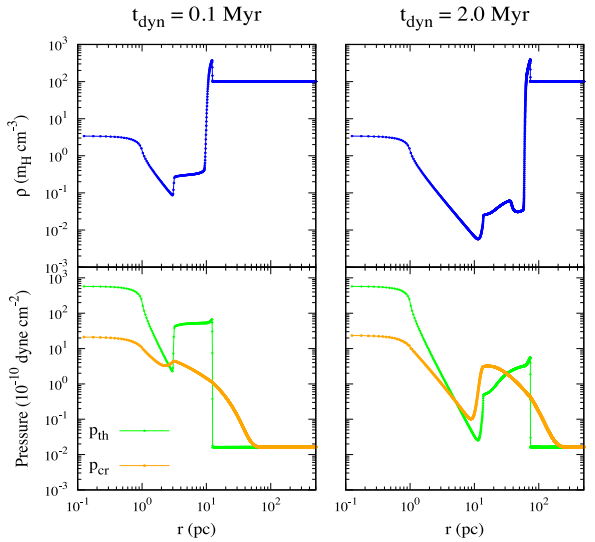

Figure 5. The snap shots of the density and pressure profiles at $t_{\rm dyn} = 0.1$ Myr (left-hand panel) and $t_{\rm dyn} = 2.0$ Myr (right-hand panel). Top and bottom panels show the density and pressure profiles. This figure highlights the energy exchange between the thermal and non-thermal (CR) fluid at the reverse shock, and shows a smooth reverse shock at $t_{\rm dyn} = 2$ Myr $> \tau_{\rm cri} = 1.7$ Myr, consistent with equation (19).

Fig. 4 plots $\tau_{\rm acc}$ as a function of dynamical time for FS and RS where CR diffusion constant is taken as $\kappa_{\rm cr} = 5 \times 10^{26}\,{\rm cm^2\,s^{-1}}$. The dotted and dashed-dotted lines represent the analytic estimate of acceleration time (i.e. equation 32), and superposed on that, the blue solid and empty circles represent the simulation result for the respective shocks. This figure shows that $\tau_{\rm acc}$ is longer than $t_{\rm dyn}$ for the FS. This is so because the velocity of the upstream and downstream flow is very small (at least a factor of ten compared to RS) and decreases with time. Therefore, a globally smooth solution is not achieved although it satisfies the upstream condition of the steady-state model by Becker & Kazanas (2001). We conclude that for a globally smooth solution, the condition is $\tau_{\rm acc} \ll \tau_{\rm cri} < t_{\rm dyn}$. This criterion limits the choice of $\kappa_{\rm cr}$ which is discussed in Section 5.1. Our two-fluid simulation results are consistent with this conclusion and the results are shown in Fig. 5.

Fig. 5 shows the snapshots of density and thermal/CR pressure profiles at two different dynamical times. During the early evolution, the RS Mach number is less than 12.3 (see Fig. 3) and therefore the upstream CR does not dominate over the thermal pressure. As time evolves, after $\tau_{\rm cri}$, the gas Mach number exceeds the critical value and the shock becomes dominated by the CRs. This CR dominated shock is a representative of a globally smooth solution as first predicted by Drury & Volk (1981). In this case, the maximum CR pressure ($p_{\rm cr,\,max}$) in the SW region depends on the input source parameters, the ambient density and the dynamical time. We have found that, $p_{\rm cr,\,max}$ does not exceed the thermal pressure for the one-fluid ISB (i.e. $p_{\rm cr,\,max} \leq P$; see equation 5), consistent with the total energy conservation.

The results discussed in this section do not include radiative cooling and thermal conduction, i.e. all the changes are only due to CRs. We will discuss more realistic cases below.

4.3 Towards a realistic model

In the previous section, we have seen that the energy exchange between thermal and non-thermal particles becomes significant at

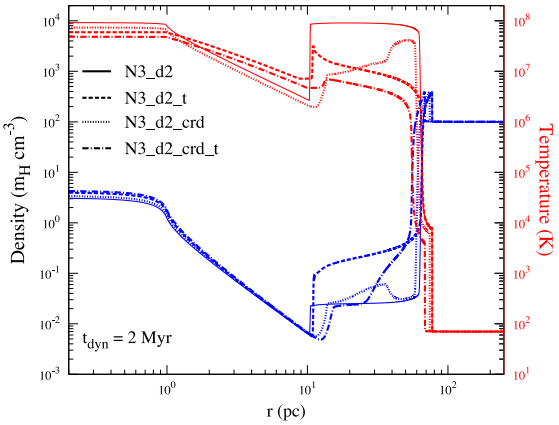

Figure 6. ISB profile with and without thermal conduction. The blue and red curves show density and temperature profiles, respectively. Each line style represents a specific model (see Table 2). For two-fluid ISB models, CRs have been injected in the driving source and CR diffusion is on. Figure shows that CRs diminish the effect of thermal conduction.

the reverse shock. We have also noticed that when $p_{cr} \gtrsim p_{th}$, the cosmic ray fluid starts affecting the inner structures (see Fig. 5). For a radiative bubble, energy loss from the dense shell reduces its thermal energy. Therefore, we expect to see the impact of CRs at an earlier time than that in the adiabatic case. In order to get a more realistic picture, we discuss the role of thermal conduction and then we turn on radiative cooling.

4.3.1 *Effect of thermal conduction*

To discuss the role of thermal conduction in CR affected ISBs, we present a comparison of one-fluid and two-fluid models. Fig. 6 displays the density (blue curves) and temperature (red curves) profiles at $t_{dyn} = 2$ Myr. For a one-fluid ISB, without thermal conduction (solid lines), the bubble temperature is high ($\sim 10^8$ K). With thermal conduction (dashed lines), the temperature drops to $\sim 10^7$ K and the SW density increases. For a two-fluid ISB, the temperature is noticeably smaller than a one-fluid ISB *even without thermal conduction* (dotted lines). With thermal conduction, it does not show a significant difference, except that, it smoothens the temperature near the CD (dash-dotted lines). Therefore, we conclude that CRs reduce the effect of thermal conduction. We have reached the same conclusion for ISBs with radiative cooling. In the following sections, we continue our discussion without thermal conduction.

4.3.2 *Volume-averaged quantities*

Fig. 7 displays the volume-averaged hot gas ($>10^5$ K) pressure and the CR pressure as functions of time for various models. The solid and empty circles display the thermal and CR pressure, respectively. The black solid lines (top curve: adiabatic and bottom curve: radiative) display equation (7) ($\gamma = 5/3$, $s = 0$), where the shell velocity is estimated from the simulation. In this case, the analytical result agrees with the simulation (as shown by the concurrence of red points with the top black line and green points with the bottom black line). For two-fluid ISBs (yellow and blue curves), as time evolves, the thermal pressure deviates from this relation. This deviation is mainly because in a two-fluid ISB, a major fraction of the free-wind kinetic energy goes to CR.

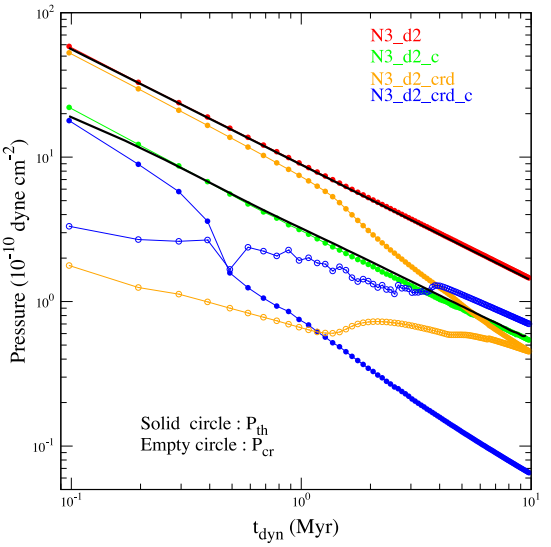

Figure 7. Time evolution of volume-averaged hot gas pressure. The solid and empty circles denote thermal pressure and CR pressure, respectively. Different colours represent the results for different models (see Table 2). Black and grey lines display the expected (equation 7) thermal pressure for a one-fluid bubble. This figure shows that the thermal pressure does not follow equation (7) for the CR affected ISB.

4.4 Evolution of different energy components

Now we come to the evolution of the kinetic/thermal/CR energy and the radiative loss for four different models. For all cases, we estimate the change of the entity x in the simulation box and normalized it w.r.t. to the total deposited energy by that epoch. These entities have been estimated using

$$\Delta E_x^t = \int_V dV\, e_x^t - \int_V dV\, e_x^0, \quad E_{IN}^t = \int_{t=0}^{t} dt\, L_w,$$
$$E_{loss} = \int_{t=0}^{t} dt \int_V dV\, n_e n_i \Lambda_N, \tag{35}$$

where x refers to the kinetic/thermal/CRs energy, E_{loss} is the radiative loss and E_{IN}^t is the total deposited energy at the source. Our results are displayed in Fig. 8.

The top panel of this figure displays the dynamical evolution of the kinetic energy (KE, red curve) and thermal energy (TE, green curve) for a one-fluid adiabatic ISB. The cooling is turned on in the second panel. In this case, the magenta curve represents the cooling losses, which shows that almost 85 − 90 per cent energy is radiated away from the ISB. Therefore, the total energy retained in the ISB is 10 − 15 per cent. One should note that this fraction may change depending on the density and metallicity of an ISM. The lower two panels show the results for a two-fluid ISB. The third panel shows the adiabatic bubble with CR diffusion and the fourth panel shows a radiative two-fluid bubble with CR diffusion. A comparison between second and bottom (magenta colour) panels demonstrates that CRs suppress cooling losses.

5 DISCUSSION

In this section, we go beyond the fiducial models and explore the parameter space (Sections 5.1, 5.2 and 5.3). We show a comparison of one-fluid and two-fluid runs, in terms of the distribution of hot gas at different dynamical times (Section 5.4). We also show the

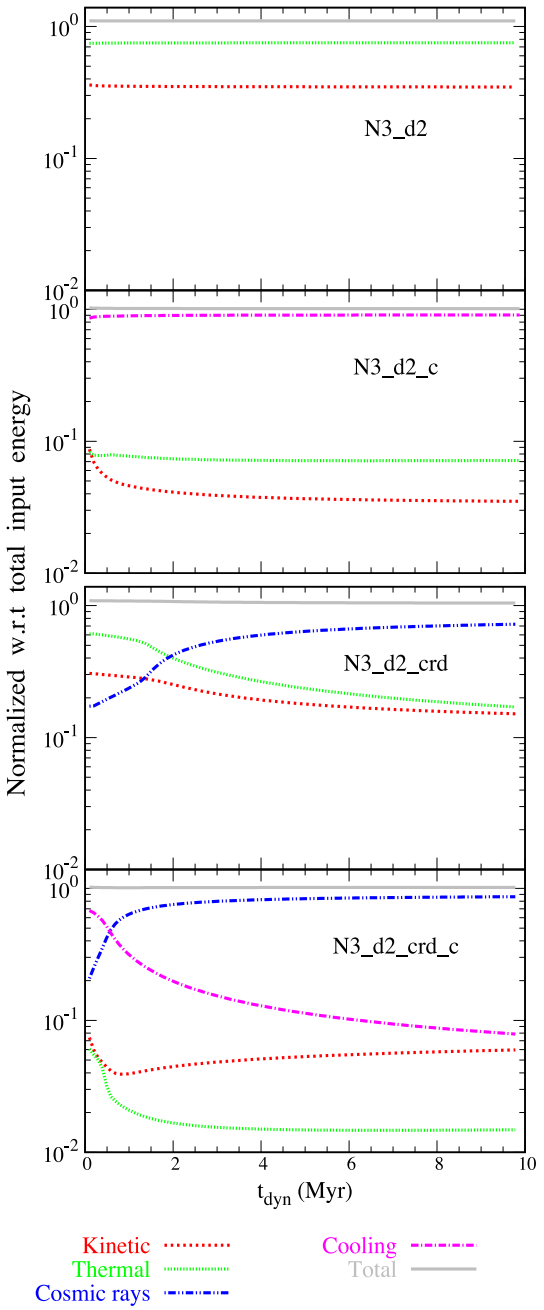

Figure 8. Time evolution of energy fraction (normalized to total injected energy) in four different cases. The upper two panels represent the adiabatic and radiative one-fluid ISB. The lower two panels stand for the adiabatic and radiative two-fluid ISB. For the two-fluid case, the CRs have been injected in the source region ($\epsilon = 0.2$). For all panels, red colour stands for kinetic energy, green for the thermal energy and blue for CR energy. The magenta colour represents radiative energy losses. This figure shows that for a two-fluid realistic case (i.e. when all microphysics are turned on; Model: N3_d2_crd_c in Table 2), CRs dominate over other energy components.

total energy gain by the CRs and discuss its dependence on various parameters (Section 5.5).

5.1 Choice of CR parameters

To begin with, we explore the parameter space of CR injection parameter ϵ_{cr}/w and diffusion constant (κ_{cr}). The CR injection parameter w (at shock, see equation 15) and ϵ_{cr} (at driving source, equation 16) are crucial parameters of two-fluid ISBs, although their origin and values are not known (Bell 2014). We treat them as free parameters. As the dependence of the result on w is easily predictable in the one-fluid model (see Section 4.2), here, we present the result for different values of ϵ_{cr} and κ_{cr}.

To visualize the dependence, we have estimated the ratio of the volume-averaged CR pressure to thermal pressure of the hot gas (temperature $>10^5$ K) and displayed them as a function of dynamical time in Fig. 9. Any point above the black horizontal line represents a CR dominated ISB.

Panel (a) shows that, for a larger value of ϵ_{cr}, the bubble becomes CR dominated at an early time. This is consistent because a larger ϵ_{cr} increases the upstream CR pressure at the reverse shock. The magenta curve of this panel shows that if $\epsilon_{cr} \lesssim 0.01$ then an ISB does not become CR dominated. A possible reason for this is the following. Pressure is a macroscopic representative of particle momenta. A small upstream CR pressure (≡small ϵ_{cr}) implies a small number of CR particles in a given momentum range. As these particles move back and forth at the shock, their momenta increase. However, if the number of the cycle and particles is not large then they cannot produce a large downstream CR pressure. A similar result is concluded by Becker & Kazanas (2001). They showed that the increase of upstream CR Mach number (in our case, at the reverse shock, it is achieved by decreasing ϵ_{cr}) can prevent CR re-acceleration (see region III of their fig. 8). Therefore, for a small ϵ_{cr}, the re-acceleration is not efficient enough for an ISB to become CR dominated.

Panel (b) shows that an ISB becomes CR dominated if $10^{26} \lesssim \kappa_{cr}/(\mathrm{cm^2\,s^{-1}}) \lesssim 3 \times 10^{27}$. If κ_{cr} is below $<10^{26}\,\mathrm{cm^2\,s^{-1}}$, then CR diffusion is almost negligible resulting in an unaffected ISB. Whereas, as κ_{cr} increases, CRs diffuse out of the ISB, and therefore a one-fluid ISB model (discussed in Section 2.1) is good enough to describe its structure.

5.2 Dependence on the ambient density

The choice of the ambient density is an important parameter while comparing the theoretical result with observations. Most of the observations provide the density of the photoionized shell, but, beyond that, it is difficult to decipher it from observations. Here, we discuss the role of the ambient density for the two-fluid ISBs.

To scan the ambient density parameter space, we select two densities: $\rho = 1\,m_H\,\mathrm{cm^{-3}}$ and $\rho = 10^3\,m_H\,\mathrm{cm^{-3}}$ (recall that our fiducial density is $\rho = 10^2\,m_H\,\mathrm{cm^{-3}}$). The nature of the ISB can be inferred from equation (19), which states that for a high ambient density, the ISB takes a longer time to attain a globally smooth solution. Simulations agree with analytic estimates as shown in panel (c) of Fig. 9. Figure shows that a lower ambient density affects the interior at an earlier time.

5.3 Dependence on N_{OB}

The dependence on N_{OB} is quite clear from equation (19). A larger number of N_{OB} correspond to a higher wind luminosity and mass-loss rate ($\tau_{cri} \propto \dot{M}^{-5/8} L_w^{-1/8} \sim N_{OB}^{-3/4}$). This means that the reverse shock can become smooth at early times. The simulation results shown in panel (d) of Fig. 9 are consistent with this. Therefore, superbubble reverse shocks, with high Mach numbers, are a promising site for CR acceleration.

One interesting point to be noted is that the ratio of P_{cr} to P_{th} is more sensitive to N_{OB} than the ambient density [compare panels (c)

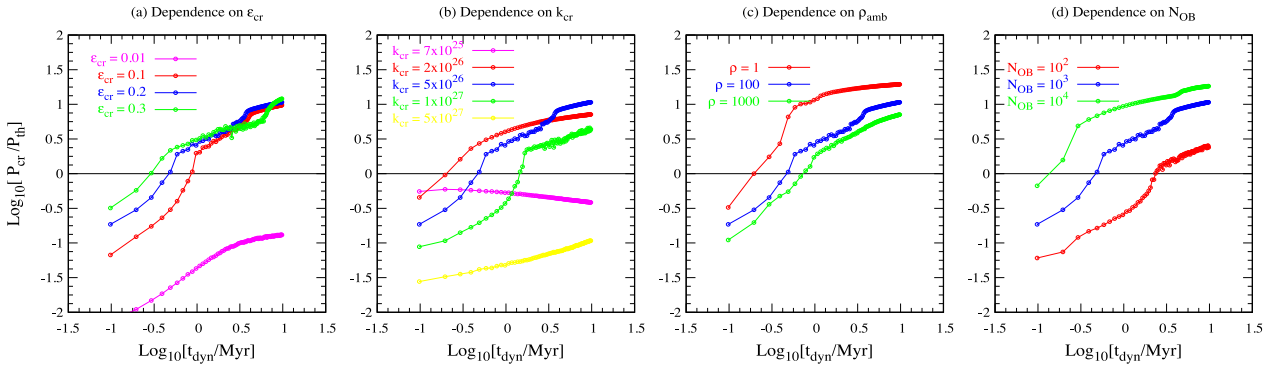

Figure 9. Comparison between the volume-averaged CR pressure and thermal pressure of the hot gas and its dependence on various parameters. The vertical and horizontal axes of all panels represent the ratio of $P_{\rm cr}$ to $P_{\rm th}$ and the dynamical time ($t_{\rm dyn}$), respectively. Any point above the black horizontal line denotes a CR dominated ISB. For all panels, the blue colour refers to the fiducial run. For all models, the radiative cooling and CR diffusion are switched on, and CRs are injected in the source region. For details, see Sections 5.1, 5.2 and 5.3.

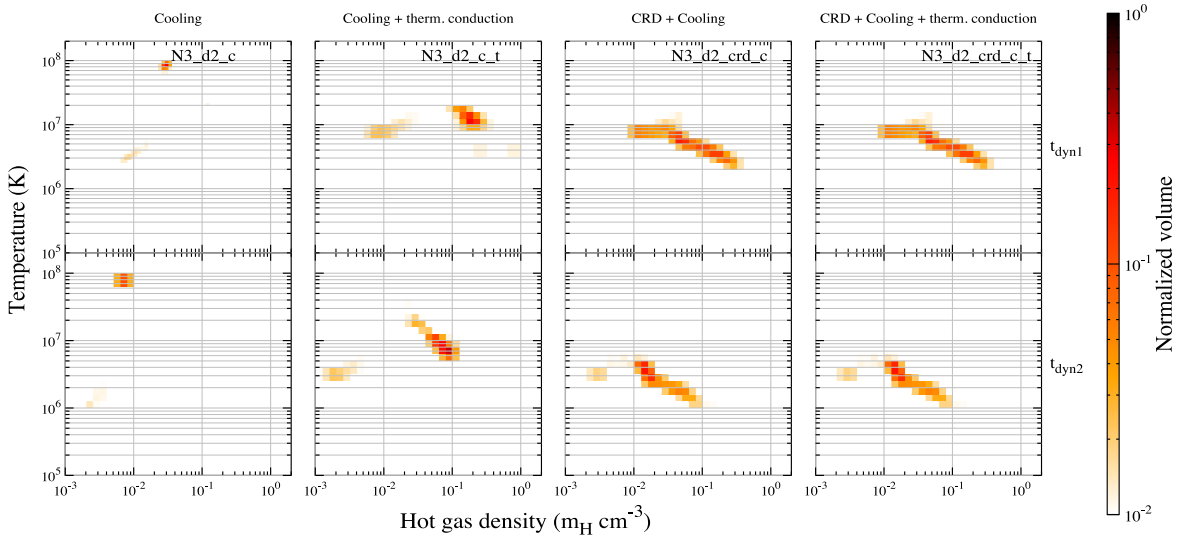

Figure 10. Comparison of hot gas properties for the one-fluid (first and second columns) and two-fluid (third and fourth columns) ISBs in the absence (first and third columns) or presence (second and fourth columns) of thermal conduction. This figure displays the snapshots of density–temperature distribution of the hot gas ($>10^5$ K) at two different dynamical times ($t_{\rm dyn1} = 0.5$ Myr and $t_{\rm dyn1} = 2.5$ Myr). Starting from the left, the first/second column represents a one-fluid ISB without/with thermal conduction, the third column displays the two-fluid model with CR diffusion (CRD) and the fourth column displays the two-fluid model with CR diffusion (CRD) plus thermal conduction. This figure shows that CR significantly affects the distribution of thermal gas inside the ISBs. We get a similar pattern for $N_{\rm OB} = 10^2$ and $N_{\rm OB} = 10^4$.

and (d)]. For example, if $N_{\rm OB}$ is lowered by two order of magnitude then the epoch of $P_{\rm cr} > P_{\rm th}$ shifts from ≈0.2 to 3 Myr and the ratio $P_{\rm cr}/P_{\rm th}$ reduces by a factor of ∼10. Whereas, the variation of ambient density by three order of magnitude changes that epoch from ≈0.2 to 1 Myr and the final ratio by a factor of ∼5. This is because, the cooling losses increase with the increase in ambient density (i.e. η is a decreasing function of $\rho_{\rm amb}$) which causes the epoch of $P_{\rm cr} > P_{\rm th}$ [i.e. $\tau_{\rm cri} \propto \eta(\rho_{\rm amb}/N_{\rm OB})^{3/4}$] to be mostly $N_{\rm OB}$ dependent. Therefore, modelling of the central source is important to obtain a CR dominated ISB.

5.4 Density–temperature distribution of hot gas

Fig. 10 shows the density–temperature distribution of hot gas. To estimate this, first, we divide the data into different density channels from $\rho = 10^{-3}$ to 2 $m_{\rm H}$ cm^{-3} ($\delta\rho = 10^{0.1}$ $m_{\rm H}$ cm^{-3}). For each density channel, we create temperature bins ($\delta T = 10^{0.1}$ K and $10^5 \leq T/{\rm K} \leq 2 \times 10^8$), and then, we calculate the hot gas volume within a given density–temperature bin. The normalization is such that the same colour corresponds to an identical volume fraction in all panels.

For all panels of Fig. 10, cooling is on. The left most panel displays a one-fluid ISB without thermal conduction. The temperature of the gas is $\sim 10^8$ K and density is low (as expected from equations 11 and 10). When thermal conduction is turned on (second panel from the left), the temperature drops to 10^7 K. In this case, the mass density is high because of the mass evaporation from the dense shell (see Section 2.1.2). Most interesting processes take place when we switch to a two-fluid ISB (third and fourth panels; $\kappa_{\rm cr} = 5 \times 10^{26}$ cm^2 s^{-1}). In this case, even without thermal conduction (third panel), the temperature drops to $(1 - 5) \times 10^6$ K. The thermal conduction (right most panel) does not show any significant difference because the lowered temperature diminishes the effect of thermal conduction. This figure shows that the CR affected ISBs can have temperatures much lower than that of a one-fluid ISB.

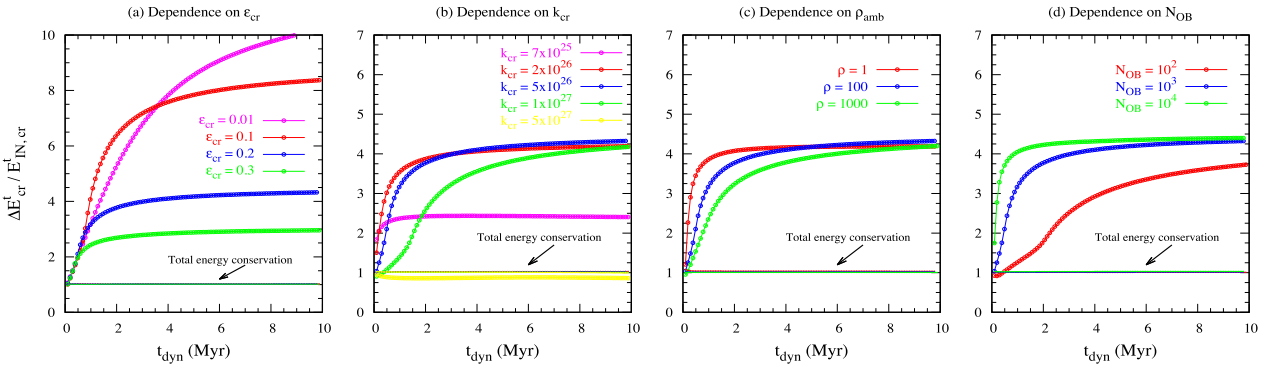

Figure 11. Time evolution of the net change in CR energy (normalized w.r.t. to the injected CR energy). For all panels, the blue curve refers to the fiducial run (for different resolutions, see Fig. C2). The horizontal lines near unity display total energy conservation in the respective runs.

5.5 Total energy gain by CRs

In previous sections, we have seen that for two-fluid ISBs, CR can gain energy from thermal particles. Here, we show the energy gain by CRs and plot it as a function of dynamical time. To the best of our knowledge, this is the first time that the net gain of CR energy (ΔE^t_{cr}) has been presented.

To obtain CR energy gain, we estimate ΔE^t_{cr} by following the same method as discussed in Section 4.4. The fraction of energy gain by the CRs $\Delta E^t_{cr}/E^t_{IN,cr}$ (where $E^t_{IN,cr} = \epsilon_{cr} E^t_{IN}$, see equation 35) and its dependence on various parameters are displayed in Fig. 11. To prevent CR outflow from the computational box (especially for the low-density ambient, large κ_{cr} and ϵ_{cr}), we set $r_{max} = 1400.1$ and choose number of grid points $n = 28\,000$ (Table 2). We have tested the total energy efficiency of the simulation box which is defined as

$$\text{Energy efficiency of box} = \frac{\sum_{x=th,ke,cr} \Delta E^t_x + E^t_{loss}}{E^t_{IN}}, \quad (36)$$

where x is the kinetic/thermal/CRs energy and E_{loss} is the radiative energy loss (also see equation 35). All the runs fulfil the energy conservation with an accuracy > 97 per cent, shown by the horizontal lines close to unity in Fig. 11.

Panel (a) of Fig. 11 shows that the CR energy gain fraction increases as ϵ_{cr} decreases. This is reasonable because at the shock the upstream kinetic energy gets converted to the downstream CR energy via CR diffusion [although the energy transfer is insufficient for it to become a CR dominated ISB; see panel (a) in Fig. 9]. This is analogous to a high Mach number one-fluid shock because the fractional change of thermal energy between the upstream and downstream flow is anticorrelated with the upstream thermal energy. In our two-fluid treatment, the upstream CR energy at the RS (and hence at FS) is set by ϵ_{cr} and CR diffusion. Panel (b) shows that CRs gain energy if $10^{26} \lesssim \kappa_{cr}/(\mathrm{cm^2\,s^{-1}}) \lesssim 3 \times 10^{27}$, consistent with the conclusion of Section 5.1. Panel (c) shows that an ISB expanding in a low-density ISM achieves maximum energy at an early time. Panel (d) confirms that a large N_{OB} can be a promising source of CRs.

6 ASTROPHYSICAL IMPLICATIONS

X-ray diagnostic is an important tool to study the interior of ISBs. Since the bremsstrahlung emissivity decreases exponentially above the gas temperature, one can find the temperature of the plasma from the X-ray spectrum. This method is very useful to determine the best-fitting temperature of the X-ray emitting gas (Dunne et al. 2003; Townsley et al. 2006; Lopez et al. 2011). The shape of spectra also tells whether emissions are coming from the thermal particles or from non-thermal particles (Dunne et al. 2003). The non-thermal emission can be used for modelling CR energy (Helder et al. 2009).

For most of the observed ISBs, the swept-up shell is quite clumpy, which allows the X-ray radiation to come out and helps one to estimate the hot gas density. The density of the hot gas is mostly obtained from the emission measure. This technique requires assuming a hot gas volume filling factor, which is taken to be $1/2 - 1$. However, we should note that this may introduce an error in the hot gas density.

The best-fitting temperature (T_x) and the density (n_x) of the X-ray emitting hot gas in the observed ISBs are given in Table 3. All these data points are taken from published results (references given in the caption of Table 3). Fig. 12 visualizes the content of this table. For all these ISBs, the dynamical age is less than 10 Myr (Lopez et al. 2014). This figure shows that the number density of X-ray gas is $n_x = (0.01\text{–}0.3)\,\mathrm{cm^{-3}}$ and the temperature is $\approx(1\text{–}9) \times 10^6$ K.

If one considers that thermal conduction is the only physical process controlling the interior temperature, then the one-fluid model can be used to explain some of the observed data points. However, as we have mentioned in Section 2, thermal conduction can be affected by magnetic fields. Alternatively, CRs can be responsible for lowering the temperature of the hot gas which diminishes the mixing between the ambient and ejecta material via evaporation. Therefore, if an observation finds that the temperature of the hot gas does not agree with the wind velocity (see equation 11) and the hot gas material is different from the ambient material (usually done by determining metallicity), then that would be a promising evidence for a CR affected ISB.

A comparison of simulation results with observations shows that the temperature matches well if CR is injected at the driving source region with a CR energy fraction $\epsilon_{cr} \sim 10 - 20$ per cent of total input energy and a CR diffusion constant $\kappa_{cr} \approx (0.1 - 3) \times 10^{27}\,\mathrm{cm^2\,s^{-1}}$. A higher value of CR diffusion constant decouples the CR energy and the thermal energy resulting in an unmodified superbubble. Therefore, if the diffusion constant is very high ($\gg 10^{27}\,\mathrm{cm^2\,s^{-1}}$), then, regardless of whether or not ISBs are sites of CR acceleration, the thermal X-ray temperature will not be a good diagnostic of the presence of CR.

In the following points, we summarize the limitations of our 1D hydrodynamic study, as applied to astrophysical systems.

Table 3. The observed ISB parameters.

Object (Name)	n_X (cm^{-3})	T_X (10^6 K)	Reference
S308*	0.28 ± 0.04	1.1 ± 0.12	[1], [2]
M17	$0.27 - 0.3$	$5.3 - 9$	[3], [5]
NGC3606	0.13	6.2	[3], [4]
Rosette	0.1	$8 - 9$	[3], [4]
30Dor	0.08 ± 0.03	4.5 ± 0.5	[3], [4], [6], [8], [10]
Carina	0.14	4.5	[3], [5], [8]
Orion	0.35 ± 0.15	1.9 ± 0.2	[9]
N4	0.28 ± 0.07	1.74 ± 0.46	[10]
N11	0.12 ± 0.02	2.32 ± 0.12	[7], [10]
N30	0.27 ± 0.09	7.78 ± 3.48	[10]
N44	0.12 ± 0.07	2.55 ± 0.813	[10]
N48	0.03 ± 0.02	6.29 ± 4.76	[10]
N55	0.01 ± 0.005	7.19 ± 1.86	[10]
N59	0.04 ± 0.02	7.31 ± 1.51	[10]
N79	0.02 ± 0.01	5.22 ± 1.39	[10]
N105	0.09 ± 0.04	2.91 ± 0.35	[10]
N119	0.06 ± 0.02	2.67 ± 0.12	[10]
N144	0.07 ± 0.02	2.90 ± 0.12	[10]
N160	0.04 ± 0.03	6.26 ± 0.46	[10]
N180	0.06 ± 0.03	3.48 ± 1.97	[10]
N206	0.05 ± 0.04	3.25 ± 0.70	[10]

[1] Chu et al. 2003, [2] Toala & Guerrero 2013, [3] Rosen et al. 2014, [4] Townsley 2003, [5] Dunne et al. 2003, [6] Pellegrini et al. 2011, [7] Maddox et al. 2009, [8] Lopez et al. 2011, [9] Gudel et al. 2008 and [10] Lopez et al. 2014. (* ISB containing two stars.)

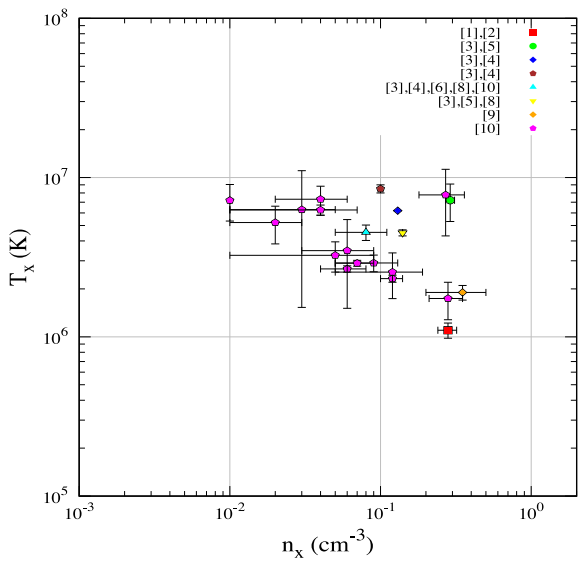

Figure 12. The best-fitting number density (n_X) and temperature (T_X) of the X-ray emitting plasma in the observed ISBs. All the plotted data points are taken from the literature (details given in Table 3). This figure shows that, for none of the ISBs, the X-ray temperature exceeds 10^7 K (≡0.86 keV).

(i) In contrast to our uniform, isotropic ambient medium, the ISM is clumpy with large density/temperature contrast between different phases. Recent 3D simulations have modelled individual SNe (instead of a superbubble driven by overlapping SNe which we are envisaging) in a more realistic clumpy ISM (e.g. Rogers & Pittard 2013; Martizzi, Faucher-Giguere & Quataert 2015; Haid et al. 2016). Reassuringly, Kim & Ostriker (2015) find that the momentum injection to the radiative shell swept-up by the blast wave and the mass in hot gas are close to that of a uniform medium with the same mean density. Therefore, we do not expect our results to change dramatically in a realistic clumpy ISM.

(ii) Our injection of stellar wind/supernova energy is also idealized. Although stars are mostly confined to a compact region in a star cluster, it will be interesting to quantify the difference in results for spatially and/or temporally distributed sources (e.g. Vasiliev et al. 2017; Yadav et al. 2017).

(iii) The ISM is magnetized and the transport of CRs and heat can be primarily along magnetic field lines. If magnetic fields are uniform then CR particles stream along the field line, i.e. $\kappa_{cr,\perp} \rightarrow 0$ and $\kappa_{cr,\parallel} >> $ Bohm diffusion coefficient (see section 2.1 in Drury 1983). However, small-scale instabilities can drastically reduce parallel diffusion of CRs (such as streaming instabilities driven by CR gradients; e.g. Kulsrud & Pearce 1969; Wentzel 1971). Similar considerations apply for thermal conduction in magnetized plasmas. In our 1D treatment, the CR and thermal diffusion coefficient should be treated as a rough ensemble average in a turbulent, magnetized ISM. CR injection is more efficient when field lines are close to parallel to the shock normal (e.g. see figure 3 in Caprioli & Spitkovsky 2014). Due to this CR injection, thermal and CR diffusion can vary along the shock depending on the orientation of the ambient magnetic field. Including these effects is beyond the scope of our idealized treatment.

(iv) The ionization, Coulombic and hadronic interaction of CR protons with thermal particles can heat up the medium (e.g. Mannheim & Schlikeiser 1994). Moreover, the streaming of CRs relative to the thermal plasma causes an irreversible transfer of energy from CRs to the thermal plasma (Guo & Oh 2008; Pfrommer et al. 2017). Efficient numerical implementation of cosmic ray streaming is still an open problem (Sharma, Colella & Martin 2010).

It is worth mentioning that, in our two fluid approach, we follow the formalism of Drury & Volk (1981) which does not include a high energy cut-off, so that large gains in the energy of pre-existing CRs may be overestimated (Eichler 1984). Therefore, a proper investigation is needed to make a complete understanding on the two-fluid equations (see e.g. Malkov & Drury 2001). In this context, another interesting course of investigation will be the comparison of a two-fluid approach with the particle-in-cell method (e.g. Bai et al. 2015; Vaidya, Mignone & Bodo 2016). These need further investigation and have been left for future work.

7 SUMMARY

In this paper, we have presented a two-fluid model of the interstellar bubbles by considering CR as a second fluid. Our work can be seen as a generalization of two standard theories of outflows: (1) CR affected blast wave (first modelled by Chevalier 1983) and (2) a one-fluid interstellar bubble (Weaver et al. 1977). The main results from this work are given below:

(i) *Dynamics without CRs*: We have found that the thermal pressure inside the bubble follows a robust relation which holds for density profile which scales as $\propto r^{-s}$ (equation 3) even with radiative cooling and thermal conduction. According to this, the volume-averaged pressure inside an ISB is $\approx \rho\, v_{sh}^2$ (see equation 7), where v_{sh} is the velocity of the expanding shell and ρ is the ambient density. Therefore, the deviation from this relation can be considered as an indication of the presence of CRs (see Fig. 7).

(ii) *CR injection and its effect*: The effect of CRs depends on (1) where the seed relativistic particles are injected and (2) what fraction of the total injected energy/post-shock pressure goes into it. Since an ISB consists of two shocks, one can inject CRs at the

forward and/or at the reverse shock. The injection at the forward shock does not change the interior structure [panel (a) in Fig. 2]. This makes ISBs different from a two-fluid SNe shock because the centre of the blast wave is dominated by CRs if the injection is done at the shock (Chevalier 1983; also see figure 1 in Bell 2014). The injection at the reverse shock can reduce the thermal pressure inside the ISB. The CR injection at shocks is described by an ad hoc parameter (denoted by w; definition is given in Section 4.2) which does not capture the actual physics of a two-fluid shock. However, a self-consistent evolution is obtained when CRs are injected in the driving source region [panel (c) in Fig. 2]. In this case, depending on the CR diffusion constant, the reverse shock can show all possible solutions of a two-fluid shock predicted by Drury & Volk 1981 (Fig. 5).

(iii) *The importance of CR diffusion constant*: The key parameter in a two-fluid model is the CR diffusion constant ($\kappa_{\rm cr}$). One can see a significant difference between the ISBs with and without CRs only if $\tau_{\rm acc} \ll \tau_{\rm cri} < t_{\rm dyn}$ (Section 4.2.2), where $\tau_{\rm acc}$ is the CR acceleration time-scale [equation (32); analogous to diffusion time-scale], $\tau_{\rm cri}$ (equation 19) is the time taken by the reverse shock to exceed the critical Mach number (Becker & Kazanas 2001) for a globally smooth reverse shock profile and $t_{\rm dyn}$ is the dynamical time. We have found that this condition is fulfilled if $10^{26} \lesssim \kappa_{\rm cr}/({\rm cm^2\ s^{-1}}) \lesssim 3 \times 10^{27}$ and in the case of ISBs with a large number of OB stars ($N_{\rm OB} \geq 10^2$) [panels (b) and (d) in Figs 9 and 11]. This supports the suggestion in the literature from phenomenological studies that massive compact stellar associations can be a promising source of CRs (Higdon & Lingenfelter 2006; Ferrand & Marcowith 2010; Lingenfelter 2012).

(iv) *Observational signatures*: An indirect evidence for the presence of CRs in ISBs can be inferred from the temperature of the X-ray emitting plasma. We have found that the CR affected bubble can have a temperature $1 - 5 \times 10^6$ K even in the absence of thermal conduction (Fig. 10) which can explain the X-ray temperature in the observed ISBs.

The model presented in this paper is admittedly idealized, which can be extended to a more realistic scenario. 3D MHD simulations of two-fluid ISBs will be important to shed further light on the question of CR origin.

ACKNOWLEDGEMENTS

We thank our anonymous referee for helpful comments. DE acknowledges support from an ISF-UGC grant, the Israel–US Binational Science Foundation, and the Joan and Robert Arnow Chair of Theoretical Astrophysics. PS acknowledges an India–Israel joint research grant (6-10/2014[IC]). SG thanks SPM fellowship of CSIR, India for financial support.

REFERENCES

Ackermann M. et al., 2011, Science, 334, 1103
Bai X.-N., Caprioli D., Sironi L., Spitkovsky A., 2015, ApJ, 809, 22
Becker P. A., Kazanas D., 2001, ApJ, 546, 429
Bell A. R., 2014, MNRAS, 447, 2224
Binns W. R. et al., 2005, ApJ, 634, 351
Blasi P., Amato E., Caprioli D., 2007 MNRAS, 375, 1471
Booth C. M., Agertz O., Kravtsov A. V., Gnedin N. Y., 2013, ApJ, 777, L16
Butt Y. M., Bykov A. M., 2008, ApJ, 677, L21
Caprioli D., Spitkovsky A., 2014, ApJ, 783, 91
Castor J., McCray R., Weaver R., 1975, ApJ, 200, 107
Chevalier R. A., 1983, ApJ, 272, 765
Chevalier R. A., Clegg A. W., 1985, Nature, 317, 44
Chu Y.-H., Guerrero M. A., Gruendl R. A., Garcia-Segura G., Wendker H. J., 2003, ApJ, 599, 1189
Chu Y.-H., Gruendl R. A., Guerrero M. A., 2003, RMxAC, 15, 62
Courant R., Friedrichs K., Lewy H., 1928, Math. Ann., 100, 32
Cowie L. L., McKee C. F., 1977, ApJ, 221, 135
Drury L. O'C., 1983, RPPh, 46, 973
Drury L. O'C., Falle S. A. E. G., 1986, MNRAS, 223, 353
Drury L. O'C., Volk H. J., 1981, ApJ, 248, 344
Dullemond C. P., 2009, Lecture on: Numerical Fluid Dynamics, Heidelberg Univ., Heidelberg, Germany
Dunne B. C., Chu Y.-H., Chen C.-H. R., Lowry J. D., Townsley L., Gruendl R. A., Guerrero M. A., Rosado M., 2003, ApJ, 590, 306
Eichler D., 1984, ApJ, 277, 429
Eichler D., 2017, ApJ, 842, 50
Ferland G. J., Korista K. T., Verner D. A., Ferguson J. W., Kingdon J. B., Verner E. M., 1998, PASP, 110, 761
Ferrand G., Marcowith A., 2010, A&A, 510, A101
Gabici S., Casanova S., Aharonian F. A., Rowell G., 2010, SF2A, 313
Giuliani A. et al., 2010, A&A, 516, L11
Gudel M., Briggs K. R., Montmerle T., Audard M., Rebull L., Skinner S. L., 2008, Science, 319, 309
Guo F., Oh S. P., 2008, MNRAS, 384, 251
Gupta S., Nath B. B., Sharma P., Shchekinov Y., 2016, MNRAS, 462, 4532
Haid S., Walch S., Naab T., Seifried D., Mackey J., Gatto A., 2016, MNRAS, 460, 2962
Harper-Clark E., Murray N., 2009, ApJ, 693, 1696
Heesen V. et al., 2014, MNRAS, 447, L1
Helder E. A. et al., 2009, Science, 353, 719
Higdon J. C., Lingenfelter R. E., 2005, ApJ, 628, 738
Higdon J. C., Lingenfelter R. E., 2006, ASR, 37, 1913
Keller B. W., Wadsley J., Benincasa S. M., Couchman H. M. P., 2014, MNRAS, 442, 3013
Kim C.-G., Ostriker E. C., 2015, ApJ, 802, 99
Kulsrud R., Pearce W. P., 1969, ApJ, 156, 445
Leitherer C. et al., 1999, ApJS, 123, 3
Li H., Chen Y., 2010, MNRAS, 409, L35
Lingenfelter R., 2012, AIP Conf. Proc. Vol. 1516, Centenary Symposium 2012: Discovery of Cosmic Rays. Am. Inst. Phys., New York, p. 162
Lopez L. A., Krumholz M. R., Bolatto A. D., Prochaska J. X., Ramirez-Ruiz E., 2011, ApJ, 731, 91
Lopez L. A., Krumholz M. R., Bolatto A. D., Prochaska J. X., Ramirez-Ruiz E., Castro D., 2014, ApJ, 795, 121
Mac Low M.-M., McCray R., 1988, ApJ, 324, 776
Maddox L. A., Williams R. M., Dunne B. C., Chu Y.-H., 2009, ApJ, 699, 91
Malkov M. A., Drury L. O'C., 2001, RPPh, 64, 429
Mannheim K., Schlickeiser R., 1994, A&A, 286, 983
Martizzi D., Faucher-Giguere C., Quataert E., 2015, MNRAS, 450, 504
Mignone A., Bodo G., Massaglia S., Matsakos T., Tesileanu O., Zanni C., Ferrari A., 2007, ApJS, 170, 228
Nath B. B., Shchekinov Y., 2013, ApJ, 777, 1
Ormes J. F., Özel M. E., Morris D. J., 1988, ApJ, 334, 722
Parizot E., Drury L., 1999, A&A, 349, 673
Pellegrini E. W., Baldwin J. A., Ferland G. J., 2011, ApJ, 738, 34
Pfrommer C., Springel V., Enblin T. A., Jubelgas M., 2006, MNRAS, 367, 113
Pfrommer C., Pakmor R., Schaal K., Simpson C. M., Springel V., 2017, MNRAS, 465, 4500
Reale F., 1995, Comput. Phys. Commun., 86, 13
Rogers H., Pittard J. M., 2013, MNRAS, 431, 1337
Rosen A. R., Lopez L. A, Krumholz M. R., Ramirez-Ruiz E., 2014, MNRAS, 442, 2701
Salem M., Bryan G. L., 2013, MNRAS, 437, 3312
Sedov L. I., 1946, JAMM, 10, 241
Sharma P., Chandran B. D. G., Quataert E., Parrish I. J., 2009, ApJ, 699, 348
Sharma P., Colella P., Martin D. F., 2010, SIAM J. Sci. Comput., 32, 3564
Sharma P., Roy A., Nath B. B., Shchekinov Y., 2014, MNRAS, 443, 3463
Sod G. Y., 1978, JCP, 27, 1

Spitzer L., Jr, 1962, Physics of Fully Ionized Gases, Interscience, New York
Stone J. M., Norman M. L., 1992, ApJS, 80, 753
Taylor G., 1950, RSPSA, 201, 159
Toala J. A., Guerrero M. A., 2013, A&A, 559, A52
Toro E. F., 2009, Riemann Solvers and Numerical Methods for Fluid Dynamics: A Practical Introduction Springer
Toro E. F., Spruce M., Speares W., 1994, Shock Waves, 4, 25
Townsley L. K., Feigelson E. D., Montmerle T., Broos P. S., Chu Y.-H., Garmire G. P., 2003, ApJ, 593, 874
Townsley L. K., Broos P. S., Feigelson E. D., Brandl B. R., Chu Y., Gamire G. P., Pavlov G. G., 2006, ApJ, 131, 2140
Vaidya B., Mignone A., Bodo G., Massaglia S., JPhCS, 719, 1
Vasiliev E. O., Shchekinov Y., Nath B. B., 2017, MNRAS, 468, 2757
Vink J., Yamazaki R., Helder E. A., Schure L. M., 2010, ApJ, 722, 1727
Wagner A. Y., Falle S. A. E. G., Hartquist T. W., 2007, A&A, 463, 195
Weaver R., McCray R., Castor J., Shapiro P., Moore R., 1977, ApJ, 218, 377
Wentzel D. G., 1971, ApJ, 163, 503
Wiener J., Pfrommer C., Oh S. P., 2017, MNRAS, 467, 906
Yadav N., Mukherjee D., Sharma P., Nath B. B., 2017, MNRAS, 465, 172

APPENDIX A: CODE CHECK

We have performed several standard test problems to check our code TFH. Here, we present two of them: (1) the shock tube problem (Sod 1978) in Cartesian geometry (Section A1) and (2) the blast wave problem (Sedov 1946; Taylor 1950) in spherical geometry (Section A2). For both cases, we present one-fluid and two-fluid solutions. We also present a test problem for the diffusion module (thermal conduction/CR diffusion) in Section A3. We have compared our results with analytical solutions and also with the publicly available one-fluid code PLUTO (Mignone et al. 2007).

A1 Shock tube

This test problem is identical to the problem described in Sharma et al. (2009) (also see Sod 1978; Pfrommer et al. 2006).

Problem set-up: We set geometry to Cartesian coordinate and choose total 2000 grid points in a domain [1, 2]. As the initial condition, the left state ($x < 1.5$) is defined as $(\rho, v, p_{\rm th}, p_{\rm cr})_{\rm L} = (1, 0, 6.7 \times 10^4, 1.3 \times 10^5)$. The right state ($x \geq 1.5$) is defined as $(\rho, v, p_{\rm th}, p_{\rm cr})_{\rm R} = (0.2, 0, 2.4 \times 10^2, 2.4 \times 10^2)$. The CFL number is set to 0.4. The snapshots of various profiles are shown in Fig. A1. The left-hand panels display the profiles for a one-fluid shock at $t = 1 \times 10^{-3}$ and the right-hand panels display the profiles for a two-fluid shock at $t = 5 \times 10^{-4}$.

A2 Blast wave

Problem set-up: We set geometry to spherical coordinate and choose total 1000 grid points in a domain [0.1, 4] pc. The initial profiles are $\rho = 1\, m_{\rm H}\ {\rm cm}^{-3}$ (uniform), $v = 0.0$ and $p_{\rm th} = (\rho/\mu m_{\rm H}) k_{\rm B} T$, where $\mu = 0.6$ and $T = 10^4$ K. At $t = 0$, at the first computational zone (say, volume $\delta V_{\rm src}$), we set energy density $10^{51}/\delta V_{\rm src}$. The CFL number is set to 0.2. The snapshots of various profiles are shown in Fig. A2. Left- and right-hand panels display the profiles of one-fluid and two-fluid blast waves where all variables are scaled w.r.t. to the self-similar variables (Chevalier 1983). For the two-fluid run, first, we identify the shock and set the CR pressure fraction to $w = 1/2$ (see equation 15). The profiles match quite well with the ODEs results (shown by black curves).

A3 Diffusion module

One useful test problem to check a diffusion module was proposed by Reale (1995).

Problem set-up: Recall their equations (15) and (16). We set $n = 5/2, a = 4.412$ and $Q = 1.2 \times 10^{15}$ K cm. The length and temperature units are defined as 10^8 cm and $\simeq 6.057 \times 10^7$ K. Total 400 grid points are uniformly set in a domain [0,5]. The initial time is chosen as $t = 0.1$ and the simulation is run up to $t = 3.1$. For a detailed set-up, see PLUTO/Testproblem/MHD/Thermal_Conduction/TCfont (Mignone et al. 2007). We turn on only the diffusion module and our results are shown in Fig. A3. For Cartesian coordinate, we have compared the results with the analytical solution (black curves in

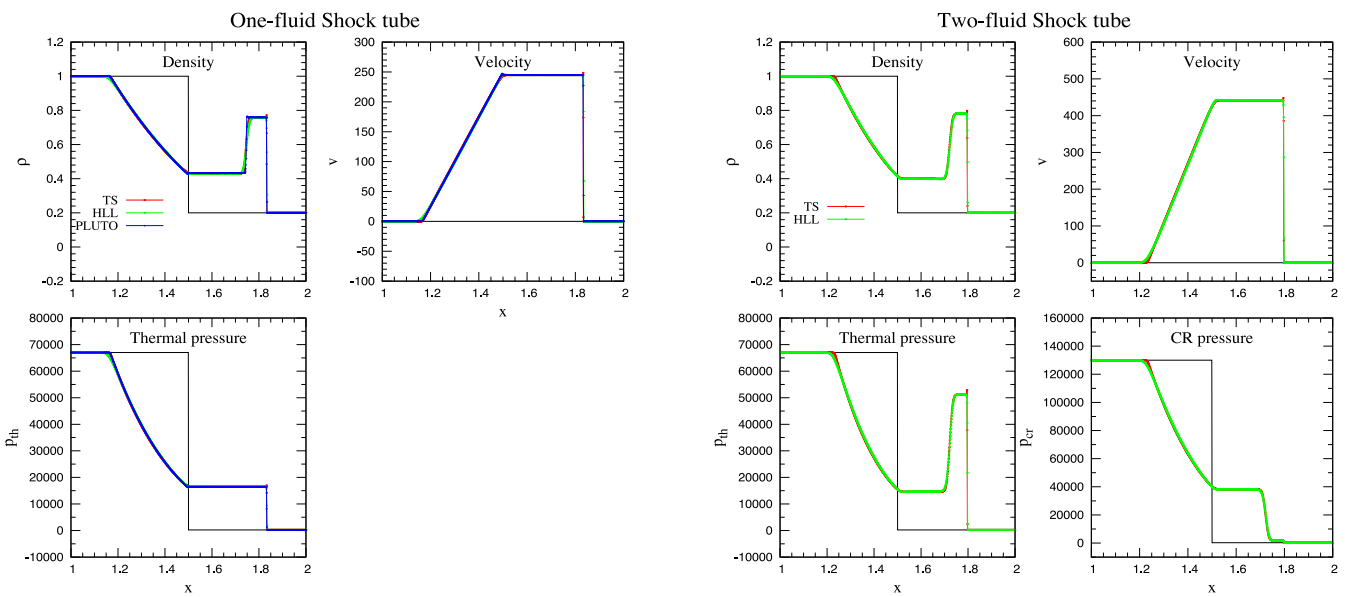

Figure A1. Shock tube: a test problem in Cartesian geometry. Left- and right-hand panels show the solutions of one-fluid and two-fluid shock tubes, respectively. Black lines represent initial profiles, blue colour stands for PLUTO, and red and green colours represent the results of 'TS' and 'HLL' solvers of the new code (TFH), respectively (described in Section 3). Figure shows that the results are quite same. For set-up details, see Section A1.

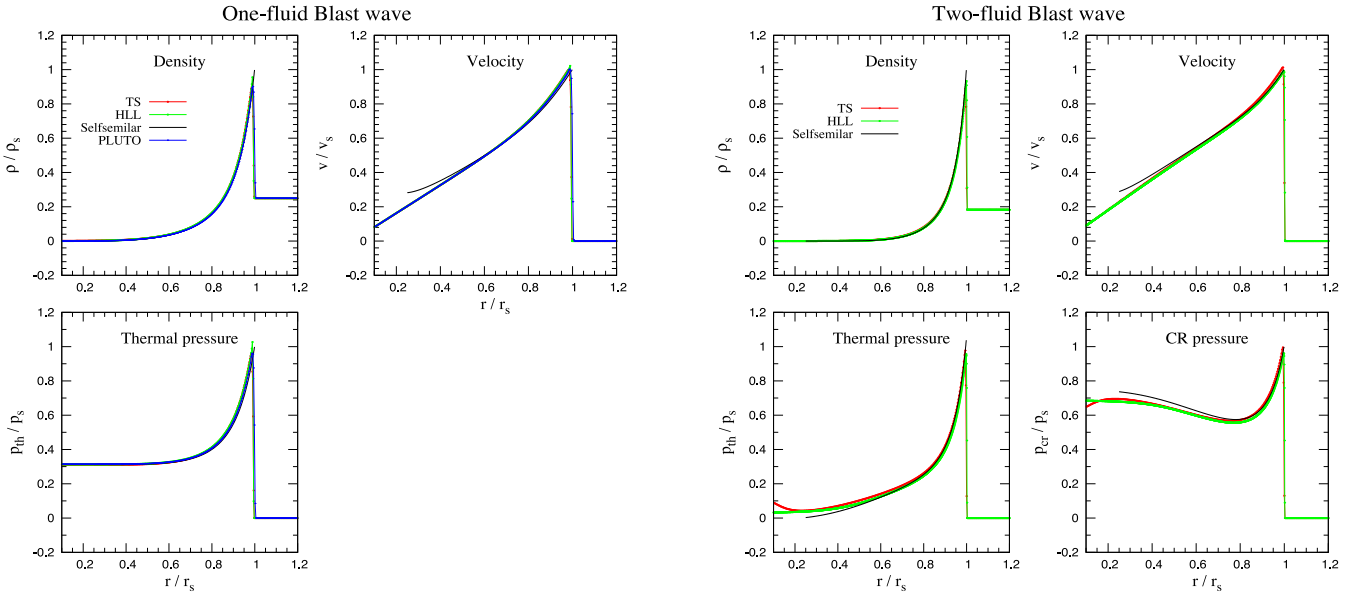

Figure A2. Blast wave: a test problem in spherical geometry. All quantities are normalized w.r.t. the self-similar variables. Left- and right-hand panels show the one-fluid/two-fluid blast wave. Black colour displays the solutions obtained from ODEs, blue colour stands for PLUTO, and red and green colours stand for 'TS' and 'HLL' solvers of our code, respectively. The numerical solutions match quite well with the analytical results.

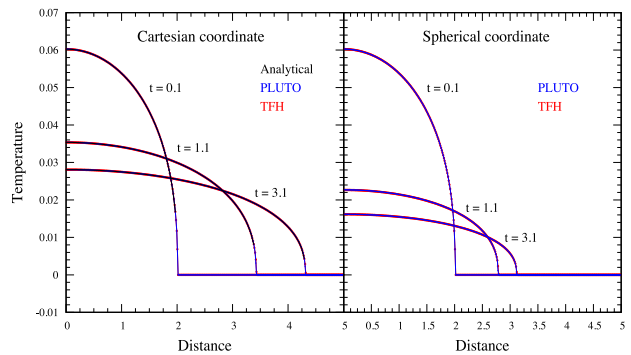

Figure A3. A test problem of diffusion module in Cartesian (left-hand panel) and spherical (right-hand panel) geometry. The black curves in the left-hand panel denote the analytical results [see equation (16) in Reale 1995]. The blue and red colours represent PLUTO and TFH output, respectively.

the left-hand panel) given in equation (16) of Reale (1995). The comparison between PLUTO and TFH is also shown in Fig. A3.

APPENDIX B: SOLVER SELECTION

TFH has two solvers: (1) TS and (2) HLL (see Section 3). Here, we show a comparison of density profile of an adiabatic one-fluid ISB at $t = 0.5$ Myr between HLL/TS solver of TFH and HLL solver of PLUTO in Fig. B1. The set-up is identical for all cases. This figure shows that first order HLL solver is more diffusive than first order TS solver explaining the reason for selecting the 'TS' solver.

APPENDIX C: RESOLUTION TEST

Here, we present the convergent tests of a two-fluid ISB by considering four different spatial resolutions: $\Delta r = 0.1$, 0.05, 0.025,

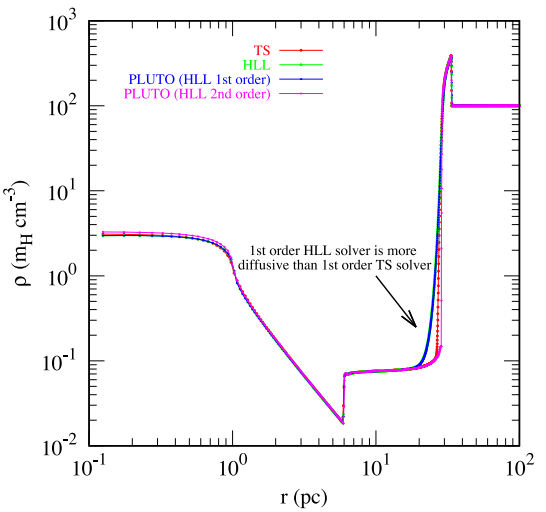

Figure B1. Comparison of ISB profiles at 0.5 Myr between PLUTO and the new code. Blue and magenta colours stand for PLUTO, and red and green colours stand for 'TS' and 'HLL' solvers of our new code, respectively. Figure highlights the reason for choosing the 'TS' solver.

0.0125 pc. Fig. C1 displays the thermal and CR pressure profiles of an adiabatic two-fluid ISB (with CR diffusion) at $t_{\rm dyn} = 0.9$ Myr and $t_{\rm dyn} = 2.1$ Myr. The blue colour in both panels denotes our fiducial resolution. This figure shows that the results are converged only for high resolutions ($\Delta r < 0.1$ pc). We have found that, the time when $P_{\rm cr} > P_{\rm th}$ increases with the decrease in spatial resolution (drastically when $\Delta r \gtrsim 0.2$ pc). A resolution test for a more realistic bubble (i.e. in addition to CR diffusion, cooling is on) is shown in Fig. C2. For our fiducial choice (resolution $\Delta r = 0.05$ pc), the results are well converged and our conclusions remain same.

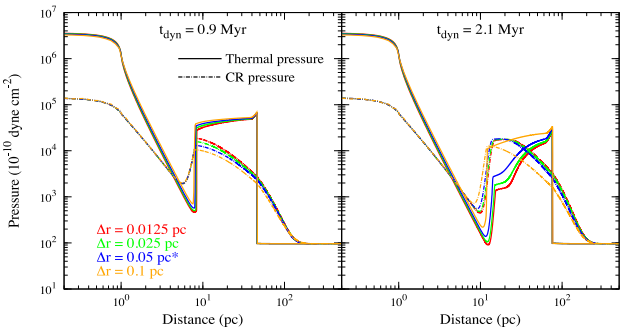

Figure C1. Resolution test: the solid lines represent thermal pressure and the dashed-dotted lines represent CR pressure profile. Left- and right-hand panels stand for two different dynamical times ($t_{\rm dyn}$ = 0.9, 2.1 Myr). For both panels, the colour code is the same. The blue colour stands for our fiducial resolution. Figure highlights that the low-resolution runs can take longer time to become CR dominated.

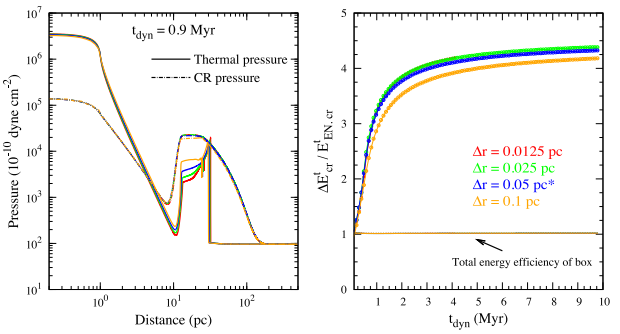

Figure C2. Resolution test for a two-fluid ISB with radiative cooling plus CR diffusion. The left-hand panel shows CR pressure (dashed-dotted lines) and thermal pressure (solid lines) profiles at $t_{\rm dyn} = 0.9$ Myr. The right-hand panel shows the net change of CR energy as a function of $t_{\rm dyn}$ (also see Fig. 11). The box size is taken as $r_{\rm max} = 1000.1$ pc, except for the red curve where $r_{\rm max} = 500.1$ pc and $t_{\rm dyn,end} = 4.1$ Myr. The colour code is the same for both panels where blue colour represents our fiducial resolution.

This paper has been typeset from a TEX/LATEX file prepared by the author.